PHILOSOPHICAL TRANSACTIONS A

rsta.royalsocietypublishing.org

Review

Cite this article: Gallaire F, Brun P-T. 2017 Fluid dynamic instabilities: theory and application to pattern forming in complex media. *Phil. Trans. R. Soc. A* **375**: 20160155. http://dx.doi.org/10.1098/rsta.2016.0155

Accepted: 3 February 2017

One contribution of 13 to a theme issue 'Patterning through instabilities in complex media: theory and applications'.

Subject Areas:
fluid mechanics

Keywords:
instabilities, pattern, free interface

Author for correspondence:
François Gallaire
e-mail: françois.gallaire@epfl.ch

Fluid dynamic instabilities: theory and application to pattern forming in complex media

François Gallaire[1] and P.-T. Brun[2]

[1]Laboratory of Fluid Mechanics and Instabilities, Ecole Polytechnique Federale de Lausanne, Lausanne 1015, Switzerland
[2]Department of Mathematics, Massachusetts Institute of Technology, Cambridge, MA 02139, USA

FG, 0000-0002-3029-1457

In this review article, we exemplify the use of stability analysis tools to rationalize pattern formation in complex media. Specifically, we focus on fluid flows, and show how the destabilization of their interface sets the blueprint of the patterns they eventually form. We review the potential use and limitations of the theoretical methods at the end, in terms of their applications to practical settings, e.g. as guidelines to design and fabricate structures while harnessing instabilities.

This article is part of the themed issue 'Patterning through instabilities in complex media: theory and applications'.

1. Introduction

Patterns are ubiquitous in nature where they are found across length scales and material properties (figure 1). Examples range from the columnar jointing in Giant's Causeway, to the ripples and dunes that form in sand, to the arrangement of seeds in many plants, to the tilling of shells protecting certain fruits and insects, to the dendritic structure of snowflakes, to the spots and stripes in many animals and insects, and to our fingerprints and the folding structure of our brain. Of particular interest in this review is the sharp contrast between the wondrous regularity of such patterns and the variety and complexity of the media that constitutes them. This singular difference suggests the existence of robust mechanisms underpinning the *genesis* of such patterns.

THE ROYAL SOCIETY PUBLISHING

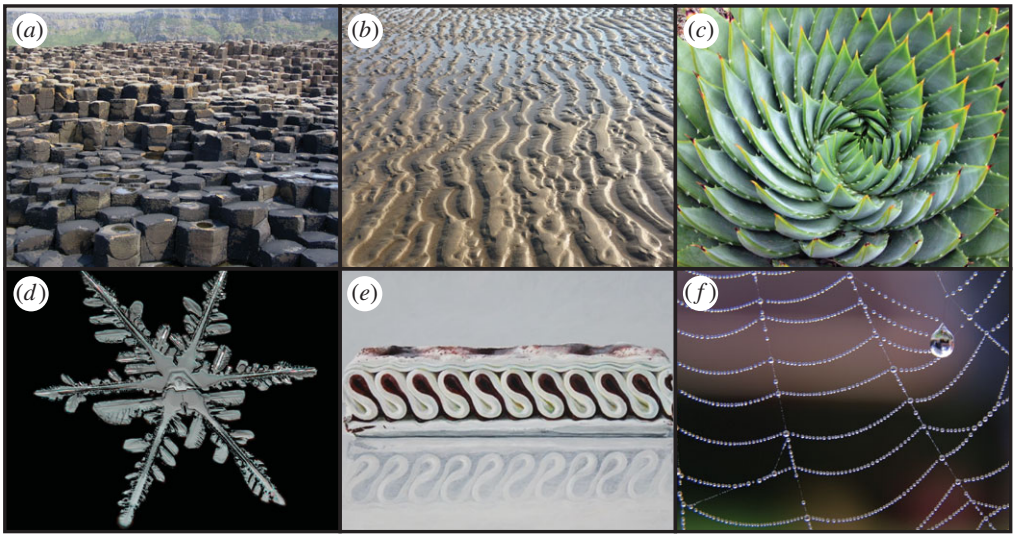

Figure 1. Patterns in nature and everyday life. (*a*) Giant's Causeway hexagonal jointing, (*b*) sand ripples in Plum Island, MA, USA, (*c*) phyllotaxis of spiral aloe, (*d*) snow flake, (*e*) Viennetta ice cream and (*f*) dew drops on a spider web. (Online version in colour.)

The question as to how patterns are formed is in fact at the crossroad of several fields, including biology, chemistry, physics, theoretical mechanics, mathematics and computer science. Efforts to rationalize their occurrence in nature date back to 1917, when D'Arcy Thompson published his pioneering book *On growth and form* [1]. He unravelled some of the generic principles at work in shaping living structures, e.g. the role played by surface tension in promoting area-minimizing surfaces. He identified the link between growth and morphology, from shells to phyllotaxis, a process later formalized and termed *morphogenesis* by Alan Turing [2], thereby creating a new field since then thoroughly explored.

Patterns, seen as the regular organization of media via tilling, branching or folding, are not exclusive to complex growing organisms and may be observed in mundane situations: when eating Vienetta ice-cakes or when observing dewdrops arranging themselves regularly onto spider webs (figure 1*e*,*f*). In such cases, patterns are the direct result of a fluidic instability and, as we shall see in the remainder of this article, their characteristic size and shapes may be elucidated using theoretical approaches. In particular, we will show how linear stability analysis may be employed to predict the wavelength of patterns in situations involving a liquid phase. Using classic instabilities such as the Rayleigh–Taylor [3,4] and Rayleigh–Plateau (see [5] for an historical note on the subject), we will exemplify how calculations made in idealized settings still qualitatively apply to complex media and how their predictive nature is, in most cases, bounded by our ability to know precisely the constitutive properties of the liquid phase. The latter observation, coupled with the growing interest in bottom-up fabrication techniques, e.g. additive manufacturing, poses a practical challenge: how patterning instabilities in complex media could reliably be harnessed as new routes of fabrications. On the one hand, the natural tendency of liquid phases to destabilize into regular structures is a critical asset driving the development of such technologies. On the other hand, the inverse problem, consisting of identifying the adequate set of initial conditions that will trigger a fluidic instability and evolve towards the desired shape without further external intervention remains an open problem for reasons that we aim to identify.

The review is organized as follows. First, we proceed to exemplify and classify the diversity of pattern-forming instabilities. We mostly focus our attention on liquid phases in the broadest sense; i.e. including ice, granular media, etc. The aim of this first part is to identify the various time

scales competing in the dynamics of pattern formation. Second, we proceed to the theoretical treatment of several archetypical free interface flows identifying the terms in the equations dictating their evolution and prescribing the characteristics of the patterns they eventually form. We do not adopt the general point of view of bifurcations and symmetry breaking [6] but rather derive the governing equations on a case-by-case basis. In this context, we highlight generic features of the structure of these equations, which help in understanding the robustness of pattern forming instabilities in liquid phases. Of course, such emerging patterns are not necessarily set in stone as they may be subject to a cascade of subsequent bifurcations yielding chaotic or turbulent behaviours. In the context of this review, we will not cover this aspect but focus on primary patterns. The instabilities considered in the article are summarized in the mosaic of figure 3. In the following sections, we progressively introduce the theoretical tools required to rationalize the outcome of such instabilities. Finally, we focus our attention on the theoretical challenges posed by our desire to use such instabilities for applications with a view to inform technological advances. Particular attention is given to the possibility to freeze patterns after their formation using a phase change.

2. Simple patterns, complex media

The word 'pattern', as used throughout this article, connotes a spatially extended structure that is periodically replicated to map the surface or the volume of a given medium. Pattern, in this sense, is the antithesis of uniformity or randomness. It suggests a notion of organization and order that does not exclude the possibility of defects and sometime chaos. As a result of this organization, a patterned medium may augment the functionality of its constituents. For example, the stripes and dots on the fur of some big cats enable their camouflage in the surrounding environment. This function could not be attained with plain furs, i.e. without pattern. Towards the goal of emulating such a function, or any other, both the shape and the typical size of a pattern are critical: the camouflage would be ruined if the stripes were as wide as the animal they cover, or else if they were too small, e.g. alternating colours on each neighbouring hair, effectively creating a new plain colour for the fur defined as the 'average' of the two initial colours. This simple observation further motivates the study of pattern formation and the rationalization of their size. Specifically, the question of the correlation between the intrinsic properties of a given medium and the characteristics of the patterns that it eventually forms is of interest in this section. Note that in the remainder of this article, we focus on inert matter, by opposition to living or active matter, and aim isolate some key ingredients of pattern formation.

(a) Phase change

Tightly intertwined with the concept of pattern formation in complex media is the notion of phase change: a phase transition as observed when water freezes/melts, a significant change in material properties following a chemical reaction (e.g. polymerization), cooling, or occurring through plasticity or fracture. Such phase changes may serve to harness the pattern formation and 'freeze' the resulting structures, or else may be triggering the pattern formation.

Let us consider a medium, capable of such a transition, subject to a set of constraints, e.g. temperature gradients, radiation, gravity, erosion, etc. These constraints may be permanently applied or vary in time thus introducing a *time scale* in the problem. In this section, we aim to classify patterns relative to the dynamics of their formation, which can either be simultaneous with or independent of the phase change (figure 2).

(b) Intrinsically coupled systems

Snow penitentes are elongated structures of hardened snow found in high altitude, i.e. in sublimation conditions. Shown in figure 2*a* is a field of such structures patterning the surface

Figure 2. Patterns obtained after a phase change: (*a*) Atacama desert's penitentes, (*b*) icicles [7] (see http://www.physics.utoronto.ca/Icicle_Atlas/), (*c*) oscillating crack in a thin film [8] (photo credit: Joel Marthelot). (Online version in colour.)

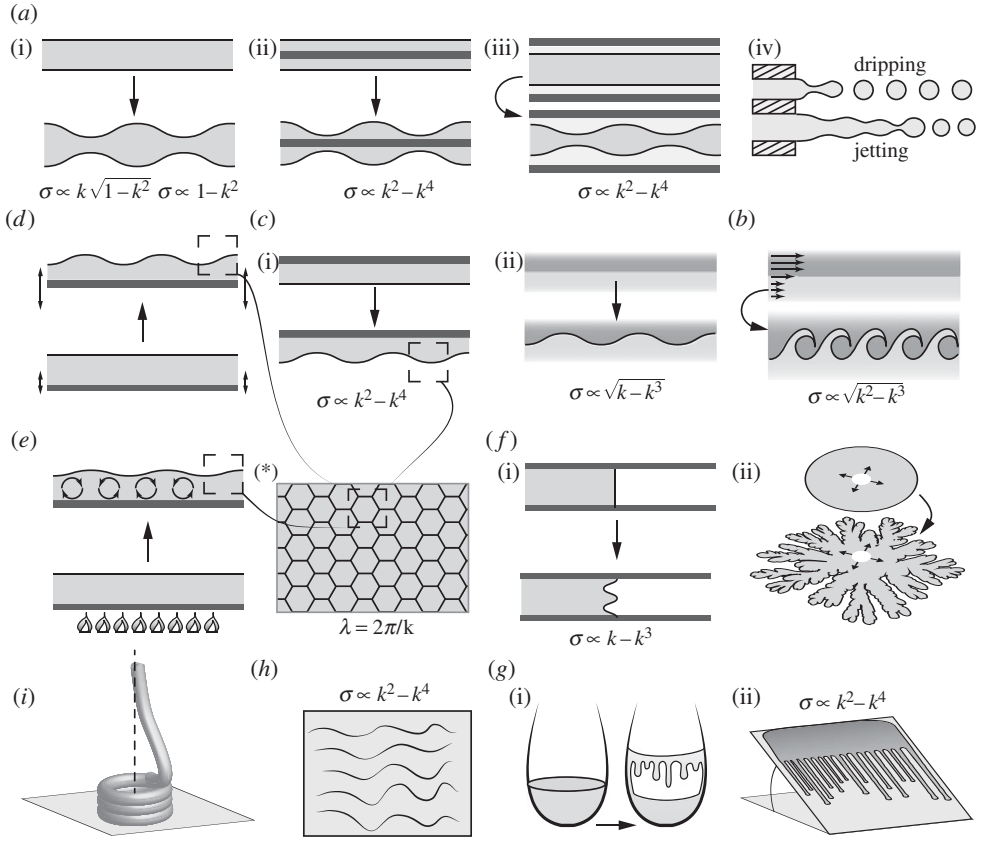

Figure 3. Sketch of the interfacial instabilities discussed in this review. The dispersion relation, σ is the growth rate and k the wavevector, is provided when available and the indices (*a*–*g*) have been chosen to match the organization of §3. (*a*(i)–*a*(iv)) Plateau–Rayleigh instability, (*b*) Kelvin–Helmoltz instability, (*c*(i),*c*(ii)) Rayleigh–Taylor instability in two-phase flows and in a thin layer, (*d*) Faraday waves arising in a bath subject to periodic oscillatory forcing, (*e*) Rayleigh–Bénard–Marangoni instability obtained when heating up a thin layer of fluid, (*) hexagonal tilling, (*f*(i),*f*(ii)) plane and radial Saffman–Taylor instability in a Hele-Shaw cell, (*g*(i),*g*(ii)) capillary ridge instability and wine tears, (*h*) Kapitza waves and (*i*) viscous coiling, with the last three being examples of instabilities found in everyday life. (*c*(ii)), (*d*) and (*e*) typically arrange in patterns such as shown in (*).

of the Atacama desert. Snow penitentes were first reported in the literature by Darwin in 1839, yet, a full-fledged model accounting for their formation has only recently been proposed [9]. A possible explanation of this time lapse lies in the intricacy of the mechanisms leading to the penitente formation: sublimation, vapour diffusion, heat conduction—all triggered by the

incident light—are tightly intertwined in the reported model. In particular, the material albedo is such that a fraction of the incoming light is reemitted, part of which impacts the surface again, giving rise to a non-trivial illumination profile at the interface. Of particular interest for our classification is that the pattern *genesis* is inherently coupled to a phase change. It is indeed through differential sublimation that the amplitude of the pattern grows over time, so that removing this feature from the problem automatically suppresses the pattern formation. In other words, those patterns are *not* the result of a *deformation of the interface*, it is instead the *ablation* of snow that permits the pattern formation. This ablation is unstable to a range of modes and the most unstable one emerges as the pattern's wavelength. This 'winner-take-all' effect is a generic feature of instabilities as discussed in §3. For now, we focus on the type of transformation that may generate patterns.

In the case of penitentes, differential ablation, via sublimation, forms the troughs and crests that eventually yield a regular pattern. Similar couplings between pattern formation and phase changes also exists when (i) some material is added; examples include differential solidification, dendrites formation in crystal growth, ripples in icicles or (ii) material is permanently displaced as through, for example, the erosion of granular media in washboarding, sand ripples or else in the fracture of a mud bed or a thin film (figure 3). Common to these examples is that patterns are formed via the *irreversible alteration* of the substrate—often at the material's interface—which therefore undergoes some sort of phase change. Theoretical developments aiming to rationalize these patterns cannot neglect this phase change, which, in general, adds to the difficulty of rationalizing them using analytical or semi-analytical tools, thereby making direct numerical approaches an important avenue of recourse.

There is however another class of problems, in which patterns do not directly arise from a phase change but rather from morphological changes of the substrate interface, while its overall integrity is retained (at least at the onset of the pattern formation). This is the case for a number of patterns in multiphase flows, free-surface flows or else for elastic substrates (shells, films, sheets, fibres, etc.) as detailed next.

(c) Towards idealized systems

Unlike the aforementioned examples, there are cases where patterns arise *without* any sort of phase transitions. We exemplify those cases which are more amenable to theoretical treatments and will serve as vehicle to derive generic features about pattern formation in §3. Examples are divided in two categories based on the nature of the substrate.

(i) Elastic substrates

In response to stress an elastic substrate may display some patterns following a morphological instability: the deformations can be focused at the substrate interface or concern its entire body (usually in slender structures). Depending on the imposed geometrical constraints and the stimuli, wrinkles, folds and creases will emerge (see [10] for a review). Note that unless the applied stresses induce some plastic deformations, the system will return to its undeformed—and thus unpatterned—state when the loading stimuli is cancelled (note that this is not necessarily possible in reality, for example if swelling was involved). These morphology changes have a rich physical landscape and an accordingly substantial range of applications. In this review, we chose not to develop this theme but instead focus our attention to fluidic problems, and in particular, to free-surface and multiphase flows.

(ii) Free-surface and multiphase flows

The creation of an interface between two materials, e.g. between two immiscible fluids, is associated with an energy cost originating from microscopic considerations [11]. Surface tension is the force per unit length that derives from this energy and dominates the physics of small enough problems, typically of the order of a few millimetres. As a direct consequence, soap films

will adopt the shape of minimal surfaces, a class of mathematical objects describing surfaces of minimal area enclosing a given volume and/or satisfying a given set of boundary conditions. Spheres, catenoids and helicoids are examples of minimal surfaces. From a mechanical point of view, surface tension—through Laplace formula—is associated with a discontinuity in the normal stress, and may induce pressure gradients in a fluid. As a consequence, equilibrium of enclosed volumes will be reached only with surfaces of iso-mean curvature under the mere influence of surface tension. The sphere is the unique solution in free space, but other shapes—derived from Delaunay curves—are possible when additional geometrical constraints are applied, for example when enclosing a drop in Hele-Shaw cell [12–14]. The question as to what occurs on the path from a sub-optimal initial configuration to a minimal or an iso-mean-curvature shape may arise. This dynamics, for example when starting from a long liquid cylinder, may give rise to singular behaviours, the breakup of the cylinder in a succession of small spheres. Capillary effects are indeed the pathway to several interfacial instability forming instabilities, albeit (i) it is not the only one and (ii) surface tension does not necessarily act alone (viscous forces, gravity, etc. often play a role too). This type of purely fluidic instability—by opposition to systems involving a phase transition—is often relatively simpler to model than the coupled systems introduced in §2a, while providing rich physical landscape including pattern formation. We therefore focus on such problems to illustrate the theoretical tools usually employed to tackle instabilities and predict their outcome. Specifically, we (i) show how stability analysis—in incremental degrees of refinement—can successfully predict the wavelength of instability mediated patterns in most cases and (ii) exemplify its intrinsic limitations as well as its future challenges.

3. From stability to pattern

In this section, we review several interfacial instability mechanisms drawing their origin in different driving forces. We use the Rayleigh–Plateau capillary instability as vehicle to introduce the theoretical approach referred to as linear instability analysis. This method aims to unravel the link between the growth of disturbances in space and in time, and the growth of instabilities in open flows with finite streamwise extension. We then briefly turn to the instability of a vorticity sheet separating two immiscible fluids flowing at different velocities, called the Kelvin–Helmholtz instability, before describing the instability of an interface surmounted by a heavier fluid than the lower one, referred to as the Rayleigh–Taylor instability. We use its variant in the case of thin fluid film to illustrate the richness of patterns that can appear in systems with two invariant directions.

We then turn to the inverse situation of a heavy thin layer of fluid surmounted by air, but which is now destabilized by a parametric vibration of the support acting like a parametrically oscillating gravitational acceleration. The stability analysis of the so-called Faraday instability requires a weakly nonlinear analysis which is described (a numerical approach is needed if one wants to explore higher amplitudes). Next, the Rayleigh–Bénard–Marangoni convection instability is discussed. Unlike the aforementioned instability, this problem has to be solved using a numerical discretization scheme in order to obtain the dispersion relation. As such, this case serves as an interesting example to illustrate the power of weakly nonlinear analysis in pattern formation.

We then turn to instabilities giving rise to fingering patterns (less regular than their hexagonal counterpart). This category includes the Saffman–Taylor instability in a Hele-Shaw cell. We describe the underlying physical mechanism and associated dispersion relation that governs the destabilization of a planar front. We briefly describe this fingering instability in radial geometry and the tip-splitting and side-branching phenomena which govern the fingering dynamics. We then turn to the fingering instability at the rim of the falling film on an inclined plane. We also briefly discuss Kapitza waves found on the surface of thin film which flows down an incline. Finally, coiling and folding of thin viscous threads and sheets are briefly described as an illustration of linear and nonlinear theoretical tools.

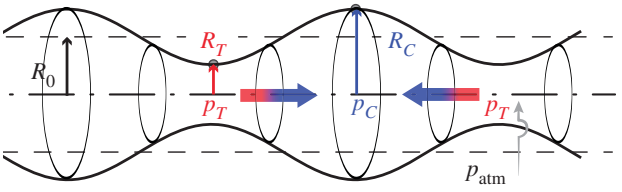

Figure 4. Physical mechanism for the Rayleigh–Plateau instability. A liquid thread of initial radius R_0 destabilizes by means of the pressure gradients imparted to Laplace law at the curved interface. (Online version in colour.)

(a) Rayleigh–Plateau instability

(i) Physical mechanism

The Rayleigh–Plateau instability refers to the instability that naturally turns a liquid thread into a series of droplets (see [5] for a complete review). On a historical note, it was first described by Savart who observed that the most unstable wavelength was approximately 10 times longer than the thread radius R_0. Plateau then later made the connection between this observation and the role of surface tension. Using a cello to excite a liquid thread at different frequencies, he found that droplets would only form if the thread was longer than approximately 1.5 times its radius $L/R_0 > 1.5$. This observation is in excellent agreement with the critical length $3R_0/2$ found by a static energy analysis of the thread (outlined next) as well as the criterion resulting from Rayleigh's hydrodynamic analysis $L > (3\pi/2)^{1/3}R_0 \approx 1.67R_0$. The same theory actually predicts that the most unstable wavelength is $9.01R_0$, in remarkable agreement with Savart's first observation.

We turn to describe the physical mechanism governing the instability. As often with capillary phenomena, two interpretations may be provided: one associated with surface energy and one related to an equilibrium of forces. This duality originates in that surface tension may indeed be interpreted as an energy per unit surface as well as a force per unit length. On an energetic standpoint, one can argue that—over the course of the instability—the system naturally evolves from a local surface energy minimum, the cylindrical thread, into a more favourable surface energy minimum, a collection of spheres, by transiently going over an energy barrier. This quasi-static interpretation is very appealing (e.g. it is easy to recover the $L > 3R_0/2$ criteria) but it is difficult to formally justify. Fluid flows are out-of-equilibrium dissipative systems and one cannot simply define a total free energy for the system.

An alternative force-based dynamical description can be provided. Imagine that the interface is slightly displaced from its nominal cylindrical shape R_0 into a wavy shape $R(x)$ with crest C and a trough T (figure 4). The points C and T are sufficiently distant: the typical wavelength of the disturbance is large compared with the radius of the thread (long-wavelength approximation $\mathrm{d}R/\mathrm{d}x \ll 1$). As such we may neglect the axial curvature κ_x with respect to the radial curvature κ_r

$$\kappa_x = -\frac{\mathrm{d}^2R/\mathrm{d}x^2}{(1+(\mathrm{d}R/\mathrm{d}x)^2)^{3/2}}, \quad \kappa_\mathrm{r} = \frac{1}{R(1+(\mathrm{d}R/\mathrm{d}x)^2)^{1/2}}, \tag{3.1}$$

so that the total curvature is approximated as $\kappa \approx 1/R$. Applying Laplace law in C and T, $p(C) = p_\mathrm{atm} + \gamma/R(C)$ and $p(T) = p_\mathrm{atm} + \gamma/R(T)$, we immediately find $p(T) > p(C)$. The pressure is therefore larger in the trough than in the crest region (this result is in stark contrast with weakly deformed elastic membranes where the pressure is larger where the membrane is inflated than where it is deflated). As a result, a pressure-driven flow accelerates the fluid from high pressure regions to low pressure regions and breaks the steady state time-invariance. The flow further empties the troughs and amplifies the crests eventually leading to the formation of droplets. Note that the eventual breakup of the thread is a complex nonlinear process (see [5] for a review). It is difficult to predict the droplet size without further mathematical modelling. One can simply

argue that (i) the only length scale in the problem is the thread radius, that (ii) from an energetic point of view, a collection of spheres has a lower surface energy than an iso-volume cylindrical thread only if the spheres have a diameter a larger than $3R_0/2$, and that (iii) the axial curvature has a stabilizing effect (it creates an overpressure in crests and an underpressure in troughs) and cannot be neglected when the wavelength becomes small. These three arguments suggest a cutoff length below which disturbances should decay so that the system will return to an equilibrium, but they fail to provide a precise wavelength selection principle. It is also difficult to identify the relevant time scale of the process without solving the dynamics of the surface-tension-driven flow. For these purposes, let us now introduce a tool, called linear instability analysis, to help in providing these dynamic selection results.

(ii) Linear instability analysis and dispersion relation

There are several terminology and notation issues when attempting to merge different studies into a review paper. Here, following [15,16], we shall distinguish the linear stability analysis of homogeneous base flows (invariant along one (say x) or two (say x, y) directions of space) and that of non-homogeneous base flows. In the first situation, a Fourier transform can be applied. This operator naturally introduces generalized waves—we shall call them normal mode perturbations—of the form $\exp(\mathrm{i}(kx - \omega t))$, where k denotes the spatial wavenumber and ω the temporal frequency. In general, $k \in \mathbb{C}$ is the complex wavenumber and $\omega \in \mathbb{C}$ the complex frequency. For classic waves, such as water waves (if one ignores viscous effects), sound waves or light waves, k and ω are real $(k, \omega) \in \mathbb{R}$ and the minus sign is chosen to allow a wave of positive phase velocity, $c = \omega/k$, to propagate in the positive x-direction. In the vocabulary of hydrodynamic instabilities, these pure waves are referred to as *neutral waves*, of spatial wavelength $\lambda = 2\pi/k$ and temporal period $T = 2\pi/\omega$. Herein, we are anticipating exponentially growing instabilities, so that we need to allow either ω, k or both quantities to be complex (see table 1).

Choosing $k \in \mathbb{R}$ real and allowing for complex $\omega \in \mathbb{C}$ is called *temporal instability analysis*. It corresponds to a physical situation where a spatial forcing is imposed to the flow. This forcing selects a particular wavelength and the temporal evolution of the perturbation is considered. If there is a wavenumber for which $\omega_\mathrm{i}(k) > 0$ (here i designates the imaginary part) then the disturbance grows exponentially and the flow is deemed linearly unstable. A mode with $\omega_\mathrm{i} = 0$ is called *neutral* while a mode with $\omega_\mathrm{i} < 0$ is referred to as *damped* or *stable*. Conversely, the *spatial instability theory* addresses the so-called *signalling problem*, i.e. the spatial development of perturbations resulting from a pointwise harmonic forcing at a given forcing frequency $\omega \in \mathbb{R}$. In contrast with the temporal stability question, we will see that the signalling problem can be ill-posed. The effective response of the system to an external forcing can be overshadowed by the natural unforced growth. This growth is captured when considering both $(k, \omega) \in \mathbb{C}$, a theory called *spatio-temporal stability theory*. Such a situation, where the spatial stability problem is ill-posed, is referred to as an *absolute instability*. It is also interpreted in §3a(vi) as a *globally unstable* flow, where the forced response is only algebraically amplified while the unforced response grows exponentially without bounds (in the linear limit). The reverse situation, where the autonomous part of the response eventually decays as it is swept away by the flow, and where the forced response dominates the flow dynamics is referred to as a *convective instability*. In §3a(vi), we refer to this problem as a *globally stable* flow. The forced response survives to the transient evolution of the ultimately decaying unforced response. As pointed out earlier, the *a priori* distinction between absolutely and convectively unstable flows requires the aforementioned spatio-temporal instability theory formalism, where both k and ω are taken complex. In conclusion, the dispersion relation, denoted $D(k, \omega) = 0$, which links k and ω for non-zero amplitude waves, may be be exploited at different levels by setting $k \in \mathbb{R}$, $\omega \in \mathbb{R}$ or keeping both quantities complex.

The dispersion relation, $D(k, \omega) = 0$, is usually obtained in four steps: (i) identify the governing equations and boundary conditions, (ii) outline the base flow, which is a solution of these equations and often a steady one, (iii) linearize the governing equations around the base flow, and

Table 1. The three different instability theories explored in this review: temporal, spatial and spatio-temporal analysis.

	temporal	spatial	spatio-temporal
wavenumber k	$\mathbb{R}$	$\mathbb{C}$	$\mathbb{C}$
frequency ω	$\mathbb{C}$	$\mathbb{R}$	$\mathbb{C}$
condition for instability	$\omega_i > 0$	$-k_i > 0$ and $\dfrac{dk_r}{d\omega} > 0$	$\omega_i(k_0) > 0$, $\dfrac{\partial \omega_i}{\partial k_i}(k_0) = \dfrac{\partial \omega_i}{\partial k_r}(k_0) = 0$

(iv) inject the normal mode decomposition $\exp(i(kx - \omega t))$ to obtain an eigenvalue problem of the form $i\omega \mathcal{B}(k)X = A(k)X$, which can be solved analytically when the number of degrees of freedom included in the unknown disturbance variable X can be reduced rigorously (as in the most cases reported in this review) or numerically when X is a discretization of the disturbance variable.

Let us now exemplify these four steps by considering the Rayleigh–Plateau instability in the inviscid limit ($Oh \ll 1$). Denoting by μ the dynamic viscosity of the fluid and by ρ its density, the Ohnesorge number $Oh = \mu/(\sqrt{\rho\gamma R_0})$ compares viscous effects and inertial effects. The Ohnesorge number is in fact the inverse of a Reynolds number where the velocity scale $\sqrt{\gamma/(\rho R_0)}$ would be capillary driven. Let us start from the depth-averaged equations governing slender jets introduced by Eggers & Dupont [17], which express the conservation of mass and momentum in the inviscid limit:

(1) Denoting $R(x,t)$ the radius of the thread, $U(x,t)$ the mean axial velocity, we write

$$\frac{dR}{dt} = -U\frac{\partial R}{\partial x} - \frac{1}{2}\frac{\partial U}{\partial x}R \tag{3.2}$$

and

$$\frac{dU}{dt} = -U\frac{\partial U}{\partial x} - \frac{\gamma}{\rho}\frac{d\kappa}{dx}, \tag{3.3}$$

in the inviscid limit $Oh \ll 1$, where κ is the total curvature. The domain extends from $-\infty$ to $+\infty$ in the streamwise direction and periodic boundary conditions can be applied.

(2) We outline $R = R_0$ and $U = U_0$ as spatially and time-independent base state. It satisfies the nonlinear governing equations.

(3) The equations are now linearized, defining $R = R_0 + \epsilon R'$ and $U = U_0 + \epsilon U'$, where $\epsilon \ll 1$ is a measure of the small perturbations,

$$\frac{dR'}{dt} = -U_0\frac{\partial R'}{\partial x} - \frac{1}{2}\frac{\partial U'}{\partial x}R_0 \tag{3.4}$$

and

$$\frac{dU'}{dt} = \frac{\gamma}{\rho}\frac{\partial}{\partial x}\left(\frac{R'}{R_0^2} + \frac{\partial^2 R'}{\partial x^2}\right). \tag{3.5}$$

(4) The time and space invariance of the base flow, together with the prescribed boundary conditions, suggest a normal mode expansion $R' = A\exp(i(kx - \omega t))$ and $U' = B\exp(i(kx - \omega t))$, which transforms the previous PDE into a 2×2 eigenvalue problem:

$$i\omega A = -U_0\, ikA - \frac{R_0}{2}ikB \tag{3.6}$$

and

$$i\omega B = \frac{\gamma}{\rho}\left(\frac{ikA}{R_0^2} + \frac{-ik^3}{A}\right). \tag{3.7}$$

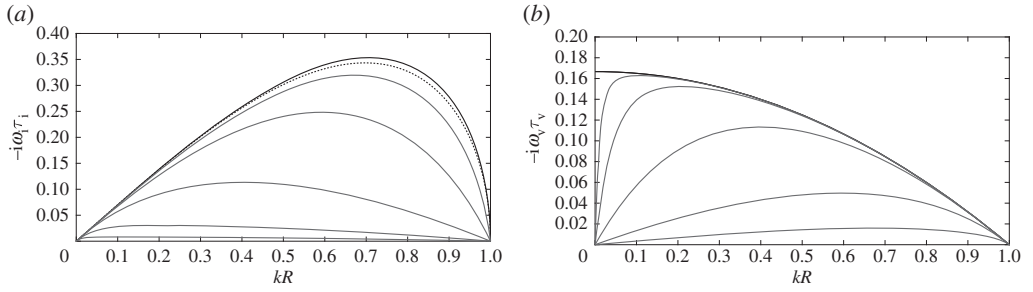

Figure 5. Dispersion relations for different *Oh* numbers. (*a*) Growth-rate $-i\omega_i\tau_i$ as a function of wavenumber *kR* in the inviscid limit from slender approximation (plain line) and from Navier–Stokes equations (dashed lines) for $Oh = 0$ and various values of $Oh = 0.05, 0.2, 1.5, 20$ in grey. (*b*) Growth-rate $-i\omega_i\tau_v$ as a function of wavenumber *kR* in the viscous flow limit limit, from slender approximation (plain line) and from Navier–Stokes equations (dashed lines) for $Oh \to \infty$ and various values of $Oh = 0.05, 0.2, 1.5, 20$ in grey.

To allow for more than the zero (trivial) $A = B = 0$ solution, the linear system should have zero determinant, which yields the following dispersion relation:

$$\omega = kU \pm i\sqrt{\frac{\gamma}{2\rho R_0^3}((kR_0)^2 - (kR_0)^4)}. \tag{3.8}$$

This dispersion relation predicts a cut-off wavenumber $k_c = 1/R_0$, which scales as the inverse of the thread initial radius, as anticipated. Equation (3.8) predicts a most unstable wavenumber equal to $k_{max} = \sqrt{2}/(2R_0)$ with characteristic growth time $\tau_i = \sqrt{\rho R_0^3/\gamma}$. This time scale reflects the effect of inertia in response to the capillary driving force. The second-order dynamics of the underlying differential equation results in the transition from an exponentially unstable/damped pair of eigenvalues for $k < k_c$ to a pair of neutral counter-propagating capillary waves when $k > k_c$. The growth rate $\omega_i(k)$ is represented by the plain line in figure 5*a* once made dimensionless with τ_i.

In the viscous limit $Oh \gg 1$, these steps are very similar:

(1) The Eggers and Dupont equations are now written:

$$\frac{dR}{dt} = -U\frac{\partial R}{\partial x} - \frac{1}{2}\frac{\partial U}{\partial x}R \tag{3.9}$$

and

$$0 = 3\nu\left(\frac{2}{R}\frac{\partial R}{\partial x}\frac{\partial U}{\partial x} + \frac{\partial^2 U}{\partial x^2}\right) - \frac{\gamma}{\rho}\frac{d\kappa}{dx}, \tag{3.10}$$

with periodic boundary conditions and where $\nu = \mu/\rho$ is the kinematic viscosity.

(2) The base state $R = R_0$ and $U = U_0$ is unchanged.

(3) Introducing $R = R_0 + \epsilon R'$ and $U = U_0 + \epsilon U'$, the linearized equations are

$$\frac{dR'}{dt} = -U_0\frac{\partial R'}{\partial x} - \frac{1}{2}\frac{\partial U'}{\partial x}R_0 \tag{3.11}$$

and

$$-3\nu\frac{\partial^2 U'}{\partial x^2} = \frac{\gamma}{\rho}\frac{\partial}{\partial x}\left(\frac{R'}{R_0^2} + \frac{\partial^2 R'}{\partial x^2}\right). \tag{3.12}$$

(4) Considering a normal mode expansion $R' = A\exp(\mathrm{i}(kx - \omega t))$ and $U' = B\exp(\mathrm{i}(kx - \omega t))$ we find

$$\mathrm{i}\omega A = -U_0 \mathrm{i}kA - \frac{R_0}{2}\mathrm{i}kB \tag{3.13}$$

and

$$0 = -2\nu k^2 B + \frac{\gamma}{\rho}\left(\frac{\mathrm{i}kA}{R_0^2} + \frac{-\mathrm{i}k^3}{A}\right), \tag{3.14}$$

which yields the following dispersion relation:

$$\omega = kU_0 + \mathrm{i}\frac{\gamma}{6\mu R_0}(1 - (kR_0)^2). \tag{3.15}$$

The first-order dynamics of the underlying differential equation results in the transition from one exponentially unstable mode into an exponentially damped one at the cut-off wavelength, precluding the existence of pure neutral capillary waves. The characteristic time of growth is $\tau_\mathrm{v} = \mu R_0/\gamma$ as a result from the hindering of the surface tension effects by viscous dissipation. While the cut-off wavelength remains unaltered by viscous effects, $k_\mathrm{c} = 1/R_0$, the dispersion relation (3.15) predicts that the most unstable wavelength diverges to infinity. In this pure viscous limit, infinite wavelengths become favoured, as evident from the plain line in figure 5*b*. This singular behaviour is imputable to neglecting inertial effects altogether, while they eventually become important when the length scale of the disturbance $\lambda = 2\pi/k$ increases without bound as $k \to 0$. Improved dispersion relations including a finite amount of inertia ($Oh = 20, 5, 1, 0.2, 0.05$) are shown in figure 5*b* for comparison. They predict a finite (though very small for $Oh = 20$) most unstable wavenumber k_max.

Both (3.8) and (3.15) are approximations of the exact dispersion relations found by the linearization of the axisymmetric Euler and Stokes equations, respectively, which both involve Bessel functions I_0 and I_1 in the dispersion relations

$$\omega = kU_0 \pm \mathrm{i}\sqrt{\frac{\gamma}{2\rho R_0^3}((kR_0) - (kR_0)^3)\frac{I_1(kR0)}{I_0(kR_0)}} \tag{3.16}$$

and

$$\omega = kU_0 + \mathrm{i}\frac{\gamma}{2\mu R_0}\frac{(1 - (kR_0)^2)}{(kR_0)^2(I_0(kR0)^2/I_1(kR_0)^2) - (1 + (kR_0)^2)}. \tag{3.17}$$

They have been included for completeness in figure 5 with dashed lines and demonstrate the accuracy of the slender Eggers and Dupont approximation. The only observable difference concerns the most unstable wavelength and growth rate in the inviscid limit, which are predicted within a couple of per cent of inaccuracy.

(iii) Variants of the Rayleigh–Plateau instability: beads and plugs

Let us mention two interesting variants of the classical Rayleigh–Plateau instability, which involve a cylindrical wire or a cylindrical tube. If one uniformly coats a cylindrical fibre with a liquid film, then the film progressively separates into alternated thick and thin regions, as seen in figures 3*b* and 1*f*, showing thick droplets hung to a spider web, after night vapour condensation. The physical mechanism originating in the above-mentioned instability remains the same: surface tension. Similarly, if one coats a hollow cylindrical tube (figure 3*c*), the inner air thread quickly destabilizes into an alternated train of lubricated bubbles and so-called liquid plugs, a situation of crucial importance in the lung. Turning back to the case of a vertical fibre where the flow is gravity-driven, the velocity profile in the thin film is close to a semi-parabola and the interface velocity $U_0 = \rho g h_0^2/\mu$ is directly related to the film thickness h_0.

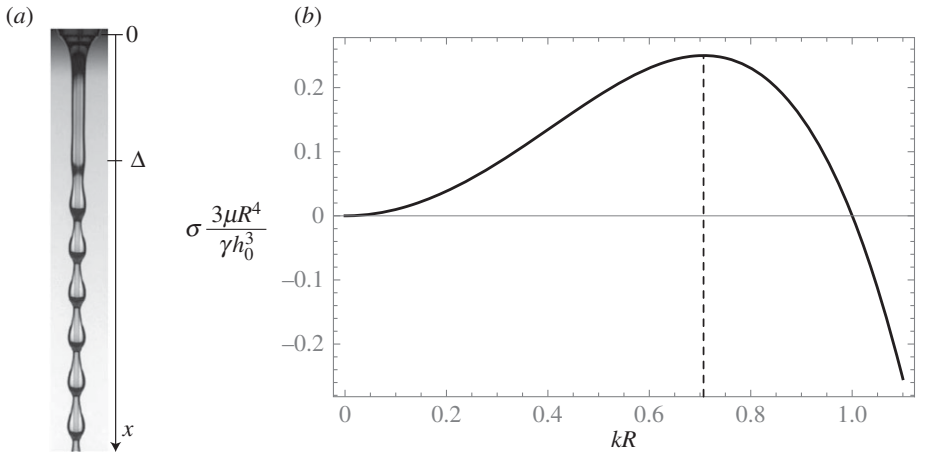

Figure 6. (*a*) Beads on a fibre (adapted from [20]) and (*b*) dispersion relation for the bead formation on the film down a fibre.

Table 2. Different Rayleigh–Plateau instabilities and their main features.

	dispersion relation $\omega =$	cut-off	λ_{max}	growth-time	$U_0^{A/C}$
$Oh \ll 1$	$kU_0 \pm \mathrm{i}\sqrt{\frac{\gamma}{2\rho R_0^3}((kR_0)^2-(kR_0)^4)}$	$2\pi/R_0$	$2\pi\sqrt{2}R_0$	$\tau_\mathrm{i}=\sqrt{\frac{\rho R_0^3}{\gamma}}$	$2\sqrt{\frac{\gamma}{\rho R_0}}$
$Oh \gg 1$	$kU_0 + \mathrm{i}\frac{\gamma}{6\mu R_0}(1-(kR_0)^2)$	$2\pi/R_0$	$\to\infty$	$\tau_\mathrm{v}=\frac{\mu R_0}{\gamma}$	$\frac{1}{3}\frac{\gamma}{\mu}$
fibre	$kU_0 + \mathrm{i}\frac{\gamma h_0^3}{3\mu R^4}((kR)^2-(kR)^4)$	$2\pi/R_0$	$2\pi\sqrt{2}R_0$	$\frac{3\mu R^4}{\gamma h_0^3}$	$1.62\frac{\gamma h_0^3}{3\mu R^3}$

In these two situations, the following dispersion relation can be obtained [18,19] assuming the layer h_0 is much thinner than the tube radius R ($h_0 \ll R$) and using the lubrication assumption:

$$\omega = kU_0 + \mathrm{i}\frac{\gamma h_0^3}{3\mu R^4}((kR)^2-(kR)^4), \tag{3.18}$$

which is shown in figure 6*b*. The dynamics of the underlying differential equation is first-order in time because, in the lubrication limit, inertial effects can be neglected with respect to viscous forces in the thin sheared layer. The effect of the destabilizing capillary pressure scaling like $(kR)^2$ is opposed by that of the transverse curvature scaling like $(kR)^4$, while viscosity sets the time scale of the instability $\tau_\mathrm{c} = 3\mu R^4/\gamma h_0^3$. Therefore, the cut-off wavenumber is unchanged $k = 1/R$ but the maximum growth-rate ω_max is attained for $k_\mathrm{max} = \sqrt{2}/2R$ (see table 2).

(iv) On the role of flow: absolute and convective instabilities

The presence of a flow has more subtle consequences than one could expect at first sight from the seemingly non-dispersive real parts of the dispersion relations (3.8), (3.15) and (3.18). The growing disturbances, which are solely growing without oscillating in the absence of advection ($U_0 = 0$) now oscillate, because of the real part $\omega_\mathrm{r}(k)$. Their oscillation in time is not limited to standing waves, but results also in oscillation is space, in strong similarity to regular neutral waves. In addition, growing perturbations of different wavelengths do not propagate at the same velocity. Still, a growing wavepacket where growth dominates over decoherence can be identified. The resulting dispersive properties are more complicated to analyse than for pure neutral waves (such as water waves, if one neglects viscous effects) and requires the concept of absolute/convective instability, to be described next.

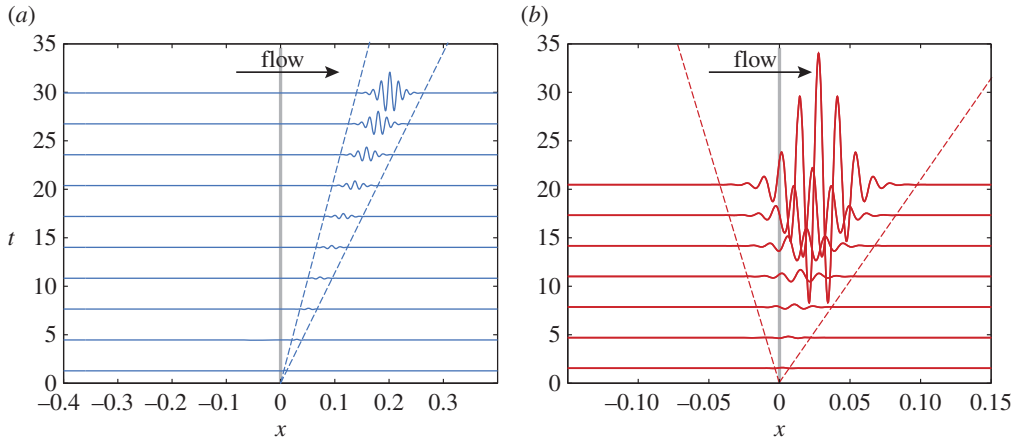

Figure 7. The wave packet evolution for (*a*) $U = 5.32$ and (*b*) $U = 0.65$ (adapted from [21]). (Online version in colour.)

In a neutrally unstable flow governed by a dispersion relation $\omega(k)$ with both $\omega \in \mathbb{R}$ and $k \in \mathbb{R}$, the evolution of a modulated wave packet at a carrier wavelength k_c is a wavepacket which travels at the group velocity $v_g(k_c) = \partial\omega/\partial k(k_c)$ and eventually disperses unless $\partial^2\omega/\partial k^2(k_c) = 0$. By contrast, linear unstable flows are self-excitable media where growth competes with dispersion. If the initial condition is temporally and spatially localized, formally taking the form of a concentrated Dirac-like impulse $\delta(x)\delta(t)$, then the coherence of the wavepacket will be preserved by the local instability and it gives rise to a growing coherent wavepacket. In the most simple cases, this wavepacket, referred to as the linear impulse (or spatio-temporal) response, is simply characterized by a trailing edge travelling at velocity v^-, a leading edge travelling at velocity v^+ and a peak of maximum growth propagating at a velocity v_{max}. These three characteristic aspects are best represented on a graph where the asymptotic growth-rate $\sigma(x/t)$ is represented as function of x/t, called the ray velocity. When the trailing edge velocities have opposite sign, disturbances will sustain their growth *in situ* in the fixed spatial reference frame (as $\sigma(0) > 0$) and eventually invade the entire flow, a situation referred to as an absolute instability. By contrast, when the edges' velocities have the same sign, growth still happens within the wavepacket but the disturbances are eventually swept away. For a given location in space, transient growth is followed by decay and the flow relaxes back to rest, a situation referred to as convective instability.

Such a situation is depicted in figure 7 using wavepackets reconstructed from the interference of all modes triggered by an initial impulse [21]. For sufficiently high values of the advection velocity (here $U_0 = 5.32(\gamma h_0^3/3\mu R^2)$), the wavepacket is swept away and the flow is only convectively unstable. By contrast, for a much smaller value of the advection velocity (here $U = 0.65(\gamma h_0^3/3\mu R^2)$), the unstable wavepacket invades the entire domain and the flow is absolutely unstable.

As reviewed in [15,16], it can be shown that v_{max} is given by the derivative of the real part of the frequency as a function of the real wavenumber in the temporal dispersion relation $v_{max} = (\mathrm{d}\omega_r/\mathrm{d}k)(k_{max})$, where the index r designates the real part. By contrast, both the spatial wavenumber k and the frequency ω have to be taken complex to determine $\sigma(0)$, the sign of which determines the convective or absolute nature of the instability. The procedure consists of identifying the admissible (see [15,16] for the necessary details) saddle point $k_0 \in \mathbb{C}$ (called absolute wavenumber) such that

$$\frac{\partial\omega_i}{\partial k_r}(k_0) = 0 \tag{3.19}$$

and

$$\frac{\partial \omega_\mathrm{i}}{\partial k_\mathrm{i}}(k_0) = 0, \tag{3.20}$$

with largest $\omega_\mathrm{i}(k_0)$ (called the absolute growth rate). Note that, under the assumption that $\omega(k)$ is an analytic function in the complex plane, Cauchy–Riemann relations imply other equivalent expressions that are preferentially chosen by some authors. It can then be shown that $\sigma(0) = \omega_\mathrm{i}(k_0)$, the sign of which decides the convective or absolute nature of the flow. The real part $\omega_\mathrm{r}(k_0)$ is called the absolute frequency. The trailing and leading edge velocities can be determined by finding $k^\pm \in \mathbb{C}$ such that

$$\frac{\partial \omega_\mathrm{i}}{\partial k_\mathrm{r}}(k^\pm) = 0 \tag{3.21}$$

and

$$\frac{\partial \omega_\mathrm{i}}{\partial k_\mathrm{i}}(k^\pm) = \frac{\omega_\mathrm{i}(k^\pm)}{k_\mathrm{i}^\pm} \equiv v^\pm. \tag{3.22}$$

Note that by virtue of the Cauchy–Riemann relations, the edge velocities are also equal to $v^\pm = (\partial \omega_\mathrm{r}/\partial k_\mathrm{r})(k^\pm)$. These properties, which define the velocity of the edges of the wavepacket, are also referred to as marginal stability criterion [22], a terminology that we shall not follow here, although it is rather popular in the pattern-forming instability community. In this review, the property of marginal stability is that of the temporal growth rate to be zero.

The absolute–convective properties can be easily determined for the three dispersion relations pertaining to inviscid and viscous jets and beads on a fibre (see table 2), although we shall only outline the derivation in this last case. The dispersion relation, once made dimensionless with time unit $3\mu R^4/\gamma h_0^3$ and length scale R is written

$$\omega = Uk + \mathrm{i}(k^2 - k^4), \tag{3.23}$$

where $U = U_0(3\mu R^3/\gamma h_0^3)$. Let us now derive the boundary between the absolutely unstable and convectively unstable domains. Denoting $k = k_\mathrm{r} + \mathrm{i}k_\mathrm{i}$ one obtains

$$\omega_\mathrm{r} = k_\mathrm{r}(-4k_\mathrm{i}^3 + k\mathrm{i}(4{k_\mathrm{r}}^2 - 2) + U), \tag{3.24}$$

$$\omega_\mathrm{i} = -{k_\mathrm{i}}^4 + {k_\mathrm{i}}^2(6{k_\mathrm{r}}^2 - 1) + k_\mathrm{i}U - {k_\mathrm{r}}^4 + {k_\mathrm{r}}^2, \tag{3.25}$$

$$\frac{\partial \omega_\mathrm{i}}{\partial k_\mathrm{r}} = 2k_\mathrm{r} + 12k_\mathrm{i}^2 k_\mathrm{r} - 4k_\mathrm{r}^3 \tag{3.26}$$

and

$$\frac{\partial \omega_\mathrm{i}}{\partial k_\mathrm{i}} = -4{k_\mathrm{i}}^3 + 2k_\mathrm{i}(6{k_\mathrm{r}}^2 - 1) + U. \tag{3.27}$$

At the saddle point, condition (3.20) applies and the two derivatives have to be zero

$$k_{0\mathrm{r}}^2 - \frac{(6k_{0\mathrm{i}}^2 + 1)}{2} = 0 \tag{3.28}$$

and

$$-k_{0\mathrm{i}} - 2k_{0\mathrm{i}}^3 + 6k_{0\mathrm{r}}^2 k_{0\mathrm{i}} = -\frac{U}{2}. \tag{3.29}$$

This system can be solved by eliminating k_{0r} and gives

$$U = -32k_{0\mathrm{i}}^3 - 4k_{0\mathrm{i}} \tag{3.30}$$

and

$$\omega_{0\mathrm{i}} = \tfrac{1}{4} - 2k_{0\mathrm{i}}^2 - 24k_{0\mathrm{i}}^4 \tag{3.31}$$

such that enforcing the absolute–convective (A/C) transition condition $\omega_{0,\mathrm{i}} = 0$ yields

$$k_{0,\mathrm{i}}^{\mathrm{A/C}} = \pm\tfrac{1}{2}\sqrt{\tfrac{1}{6}(\sqrt{7} - 1)} \tag{3.32}$$

and

$$U^{\mathrm{A/C}} = \tfrac{1}{3}\sqrt{\tfrac{2}{3}}(\sqrt{7} - 1)^{3/2} + \sqrt{\tfrac{2}{3}(\sqrt{7} - 1)} \simeq 1.62. \tag{3.33}$$

Going back to the flow parameters, the instability will be absolute if

$$U_0 < 1.62\frac{\gamma h_0^3}{3\mu R^3}. \tag{3.34}$$

Physically, this means that the domain of absolute instability increases with surface tension γ, aspect ratio h_0/R and decreases with an increasing viscosity μ.

The consequence of the transition from convective instability to absolute instability for coated vertical fibres (figure 6) has been analysed in detail by Duprat *et al.* [18,20], who have demonstrated how the disturbances changed from a broad-band distribution of disturbances to a sharp peak oscillatory behaviour. Absolute instability yields a sharp frequency and wavelength selection as well as short entry length for the saturated pattern to emerge. By contrast, the frequency spectrum is much broader and the intact length longer and more fluctuating in the convective instability case. In the words of Huerre & Monkewitz [15], this is the transition from an amplifier flow, which is condemned to amplify external disturbances, to a self-sustained oscillator flow. The link between the local absolute/convective properties of the instabilities and the global behaviour of the flow is next described.

(v) Spatial stability analysis

It should now be clear to the reader why in an absolutely unstable situation the signalling problem, in which the growth in space of the response to a sustained harmonically pulsating source at frequency ω_f located at, say, $x = 0$ is monitored, is ill-posed. Indeed, this forced response, consisting of upstream (so-called k^-) and downstream (so-called k^+) propagating branches with frequency ω_f, will be mixed with the naturally growing wavepacket which invades the entire domain (figure 7) and therefore forbids the formation of a 'stationary' regime where the forcing frequency ω_f is dictated everywhere. By contrast, the spatial instability problem is well posed when the flow is convectively unstable as the transient wavepacket eventually decays for any point x, leaving the forced waves dominating the final response.

The spatial instability problem is often more complicated to solve than the temporal stability problem. It is not because there exists an analytical expression for $\omega(k)$ that the same holds true for $k(\omega)$. More than that, because of the differential order in time and space of the underlying governing equations, it is often the case that there are more spatial branches $k^{(n)}(\omega)$ than temporal branches. For the coated cylindrical fibre, where inertia is entirely neglected, there is only a single temporal branch (3.23) while there are four spatial branches $k^{(n)}(\omega)$, $n = 1 \ldots 4$. Although they are expressed as roots of a fourth-order polynomial, they do not have any apparent analytical expression.

Another difficulty stems from the identification of the propagation direction of these waves. The sign of $k_i(\omega)$ is indeed not conclusive; it depends on whether the wave propagates in the positive $x > 0$ direction (it is then called a k^+) or in the negative $x < 0$ direction (it is then referred to as a k^- branch). The rigorous approach is to add an artificial imaginary part $\gamma > \omega_{i,max}$ to ω so as to separate the branches into the upper $k_i > 0$ and lower $k_i < 0$ planes (as $\gamma > \omega_{i,max}$, there is indeed no possible intersection of the branches with the $k_i = 0$ axis, as they would absurdly yield a temporal mode with a larger growth rate than $\omega_{i,max}$). As for such an unphysical exponentially growing forcing with time, the branches have to be damped in space, the branches located in the upper half-plane are k^+ waves and vice versa. The branches are then tracked by continuation by progressively lowering the artificial γ to 0, unless a saddle point appears at $\omega_{0,i} > 0$ if the flow is absolutely unstable.

In the present flow, we have found that there are two downstream-propagating waves and two waves propagating upstream. Among these four waves, only one of the k^+ waves was found amplified. Its growth rate $-k_i(\omega)$ is represented for various values of $U \in [U^{C/A}, 2]$ in the convective regime in figure 8*b*. One first observes that the most amplified frequency drifts to lower values with decreasing U, which illustrates the dispersive nature of the spatial stability analysis. One can also notice the formation of a cusp when U approaches $U^{C/A}$, which traduces

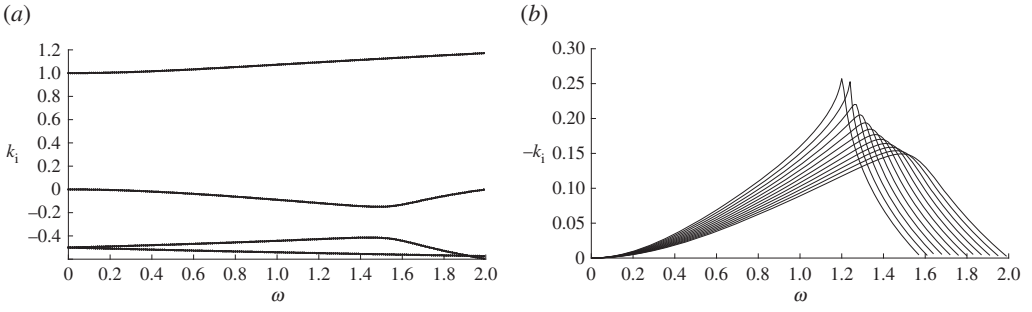

Figure 8. (*a*) Spatial branches for $U = 2$; among the two k^+ and two k^- branches, there is only one unstable k^+ mode. (*b*) Spatial growth rate as a function of the forcing frequency for different values of $U \in [U^{C/A}, 2]$.

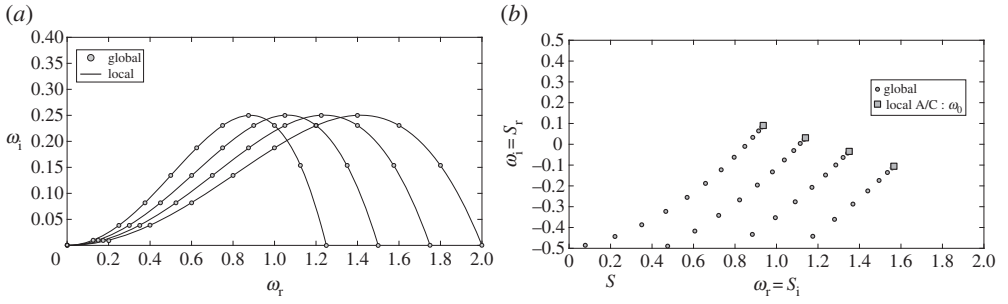

Figure 9. Global (circles) and local (continuous line and squares) eigenvalues obtained for a coated cylindrical fibre with (*a*) periodic and (*b*) Dirichlet–Neumann boundary conditions for different values of the free surface velocity $U = 1.25, 1.5, 1.75$ and 2. The size of the domain is set to $L = 20\pi$.

the incipient ill-posedness of the spatial stability problem in the absolutely unstable velocity range $U < U^{C/A}$. Such predictions are rather difficult to validate in real flows because the base flow also often evolves spatially downstream, calling for a global resolvent analysis (see §3a(vii)).

(vi) Global stability analysis

Considering an invariant base flow, say along the direction x, there is a very natural connection between the analysis of infinite version of this domain using Fourier transform through a normal mode expansion and that of its *periodic* version, say of period L. The only difference is a quantization of the possible waves which can fit into the periodic box. As seen in figure 9*a* for the reference dispersion relation of the coated fibre (3.23), the continuous dispersion relation $\omega(k)$ is replaced by a discrete set of modes $\omega(2n\pi/L)$ for $n \in \mathbb{N}^+$. The longer the box, the more modes, the shorter, the fewer until the point where the box is too short to allow the cut-off wavenumber to fit in. In addition to the ubiquitous physical situation where periodicity exists, for instance for axisymmetric base flows, periodic conditions have sometimes also been sought for in the laboratory, to avoid imposing appropriate inlet and outlet boundary conditions [23].

However, the link between the stability of the above discussed infinite x-invariant base flow and that of finite size version equipped with *non-periodic boundary conditions* is far less intuitive. Such a situation belongs to the class of global stability analysis. There is indeed an equivalence between a polynomial dispersion relation and the associated global eigenvalue problem, framed as a spatial ordinary differential equation. In contrast with the global analysis of nominally non-x-invariant flows, the invariance is here solely broken by the boundary conditions.

Without claiming for too much generality, let us point out the following two caveats, related to the choice of boundary conditions. First, the differential order alone of the resulting operator sets the number of boundary conditions, but not their location. The answer should actually be given

by the spatial analysis and one should impose as many inlet (resp. outlet) boundary conditions as k^+ (resp. k^-) waves. Second, the boundary conditions can have a dramatic influence on the resulting eigenvalues. This can even be appreciated by first considering the situation where the flow is neutrally stable and acts as a one-dimensional waveguide. It is then well known, think for instance of musical instruments, that boundary conditions can be met by superimposing two counter-propagating travelling waves. This yields a countable infinite set of global eigenvalues, which inherit the neutrality of the underlying waves. This property however only holds when the boundary conditions are unable to feed energy into the system. It is indeed also known [24] that the buckling instability of a beam can be understood as resulting from the action of energy-feeding (call them overreflecting) boundary conditions onto elastic bending waves that travel back and forth along the beam and reflect periodically on both ends. Let us insist: an infinite beam only hosts neutral (neglecting dissipation) waves ($\forall k \in \mathbb{R}, \mathrm{Im}(\omega(k)) = 0$), but a finite beam eventually buckles for realistic boundary conditions. The conditions under which this can happen and the link between the local propagation properties have been discussed in the literature, coining the concept of negative energy wave. Similar mechanisms, which do not require local instabilities to display global instability to be triggered, have been unravelled in the garden-hose instability or is suggested as a possible interpretation for vortex breakdown [25].

Even considering as transparent as possible boundary conditions, but turning to locally unstable flows, the global eigenvalues of a bounded system have not much in common with those of the same but periodic system. Consider for instance the coated fibre with dispersion relation (3.23). It is equivalent to the interfacial differential equation

$$\frac{\partial \eta}{\partial t} = -U\frac{\partial \eta}{\partial x} - \frac{\partial^2 \eta}{\partial x^2} + \frac{\partial^4 \eta}{\partial x^4}. \tag{3.35}$$

It can be rephrased into a global differential eigenvalue problem, setting $\eta(x,t) = \hat{\eta}(x)\exp(st)$

$$s\eta = -U\frac{\mathrm{d}\eta}{\mathrm{d}x} - \frac{\mathrm{d}^2\eta}{\mathrm{d}x^2} + \frac{\mathrm{d}^4\eta}{\mathrm{d}x^4}. \tag{3.36}$$

Considering that the fibre is held between two reservoirs at a fixed distance, it is not illegitimate to consider homogeneous Dirichlet–Neumann boundary conditions $\eta(0) = \eta(L) = 0$ and $(\partial\eta/\partial x)(0) = (\partial\eta/\partial x)(L) = 0$. The resulting global stability problem can be easily solved numerically upon discretization of the x interval $[0, L]$. For a value of $L = 20\pi$ (L should not be taken too large with finite arithmetic computers as the associated eigenmodes exponentially grow in space), the obtained eigenvalues are reported in figure 9*b*. They are aligned on a line that emanates from the absolute frequency ω_0. This analysis shows the link between the absolute/convective properties of an infinite flow and the global stability properties in the presence of boundary conditions that break streamwise invariance.

This link between absolute/convective instability properties and global stability is best formalized and understood by considering an approximate dispersion relation. By definition of the saddle point k_0, the dispersion relation locally is written

$$\omega = \omega_0 + \alpha_0(k - k_0)^2, \tag{3.37}$$

where $\alpha_0 = \frac{1}{2}(\mathrm{d}^2\omega/\mathrm{d}k^2)(k_0)$ is a complex coefficient. The associated model PDE is written (here $\eta(x,t)$ is a fake variable)

$$\frac{\partial \eta}{\partial t} = -\mathrm{i}(\omega_0 + \alpha_0 k_0^2)\eta + 2\alpha_0 k_0 \frac{\partial \eta}{\partial x} + \mathrm{i}\alpha_0 \frac{\partial^2 \eta}{\partial x^2}, \tag{3.38}$$

to which we add the boundary conditions $\eta(0) = \eta(L) = 0$. We seek solutions of the form $\hat{\eta}(x)\exp(st)$ where s is the global eigenvalue. We have to solve

$$s\hat{\eta} = -\mathrm{i}(\omega_0 + \alpha_0 k_0^2)\hat{\eta} + 2\alpha_0 k_0 \frac{\partial \hat{\eta}}{\partial x} + \mathrm{i}\alpha_0 \frac{\partial^2 \hat{\eta}}{\partial x^2}, \tag{3.39}$$

which have solution $\hat{\eta}(x) = \exp(lx)$ where l obeys

$$\frac{\mathrm{i}s}{\alpha_0} - \left(\frac{\omega_0}{\alpha_0} + k_0^2\right) - 2\mathrm{i}k_0 l + l^2. \tag{3.40}$$

The solutions for l are easily found

$$l = \mathrm{i}k_0 \pm \sqrt{-\frac{\mathrm{i}s}{\alpha_0} + \frac{\omega_0}{\alpha_0}}. \tag{3.41}$$

As a consequence, the eigenmode is written $\hat{\eta}(x) = a^- \exp(l^- x) + a^+ \exp(l^+ x)$, where $a^\pm$ are chosen to satisfy the boundary conditions $a^- \exp(l^- 0) + a^+ \exp(l^+ 0) = 0$ and $a^- \exp(l^- L) + a^+ \exp(l^+ L) = 0$. This imposes that $a^- = -a^+$ and $\exp(l^- L) = \exp(l^+ L)$. Therefore, $(l^- - l^+)L = 2n\pi$, i.e. $-\mathrm{i}s/\alpha_0 + \omega_0/\alpha_0 = n^2\pi^2/L^2$, which yields

$$s = -\mathrm{i}\omega_0 + \frac{\mathrm{i}\alpha_0 n^2 \pi^2}{L^2}. \tag{3.42}$$

The global eigenvalues are therefore aligned on a line emanating from $-\mathrm{i}\omega_0$ and oriented in the direction given by $\mathrm{i}\alpha_0$. In most cases, α_0 has a negative real part, as the saddle point at k_0 connects a k^+ branch stemming from the upper complex k-plane to a k^- stemming from the lower k-plane (for a counter-example, see [26]) and the global eigenvalues have therefore growth rates with upper bound ω_{0i}. Most often, absolute instability and global instability are therefore intimately related.

As a word of caution, observe that there are many hydrodynamic instability problems where fluid mechanical depth-averaging is impossible, as for example the Rayleigh–Bénard–Marangoni convection instability described in §3e. It is then not always possible to obtain a polynomial dispersion relation. This precludes the use of a one-dimensional model equation for unravelling rigorously the link between global and local spatio-temporal stability properties, although the qualitative picture is likely to remain often unchanged.

(vii) Global resolvent analysis and link with the signalling problem

Now that we have understood that the global stability properties of a flow with non-periodic boundary conditions are dictated by the absolute/convective properties of the parallel flow interpreted in the local stability framework of the parallel flow viewed in an infinite streamwise extension framework, one can reconsider the signalling problem and the spatial instability theory. It is known indeed from dynamical system theory that the linear response to an external harmonic forcing at frequency ω_f is only well defined when the linear operator is stable. If not, the solution is the superimposition of the unforced natural exponentially growing mode and the algebraically amplified solution.

We therefore consider the response of the flow to a distributed harmonic forcing $\hat{f}(x)\exp(\mathrm{i}\omega_\mathrm{f} t)$

$$\frac{\partial \eta}{\partial t} + U\frac{\partial \eta}{\partial x} + \frac{\partial^2 \eta}{\partial x^2} - \frac{\partial^4 \eta}{\partial x^4} = \hat{f}(x)\exp(\mathrm{i}\omega_\mathrm{f} t) \tag{3.43}$$

and

$$\eta(0) = \eta(L) = \frac{\partial \eta}{\partial x}(0) = \frac{\partial \eta}{\partial x}(L) = 0. \tag{3.44}$$

Looking for harmonic solutions at frequency ω_f, $\eta(x,z) = \hat{\eta}(x)\exp(\mathrm{i}\omega_\mathrm{f} t)$, the resulting resolvent equation can be formally written as

$$(\mathrm{i}\omega_\mathrm{f}\mathsf{I} + \mathsf{A})\hat{\eta} = \hat{f}, \tag{3.45}$$

where A is a spatial linear operator which includes all homogeneous boundary conditions and I the identity operator. The transfer function or gain is

$$G(\omega) = \frac{\|\hat{\eta}\|}{\|\hat{f}\|}. \tag{3.46}$$

This gain can be further maximized finding the optimal forcing structure at each forcing frequency that yields the highest possible gain [27]. In contrast with the typical multi-peaked transfer

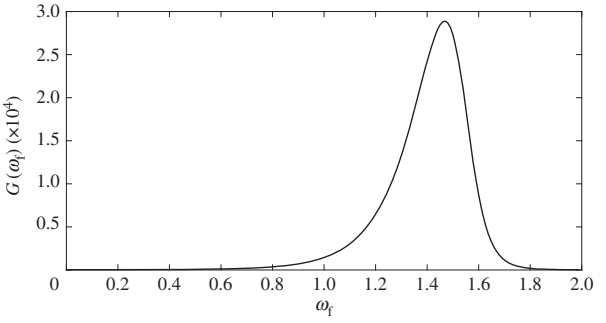

Figure 10. Optimal frequency response of a coated fibre at $U = 2$.

function of damped periodic systems (think of an organ pipe which selectively amplifies a discrete set of frequencies, the fundamental and its harmonics), the transfer functions obtained here for $U = 2$ show a single broad peak close to the most spatially amplified frequency, as seen in figure 10. Observe also that the most amplified frequency is close to $\omega_f = 1.43$, a value very close to the frequency displaying the largest spatial growth rate (figure 8*b*).

(viii) Wavelength selection mechanisms

We have now given the basic toolbox to study the linear instability of streamwise homogeneous base flows from the local stability point of view, where a local dispersion relation $D(k, \omega) = 0$ is obtained and interpreted in the temporal, spatial and spatio-temporal context and from the global point of view when boundary conditions are included and the flow has a finite streamwise extent. For three different variants of the Rayleigh–Plateau instability, the dispersion relation and its main outcomes are gathered in table 2. The resulting wavelength selection puzzle is however far from settled. With the exception of flows without mean advection, the most unstable wavenumber k_{max} is not likely to naturally emerge, despite its maximum exponential growth. By contrast, in convectively unstable flows, which behave as amplifiers, there is a most-amplified frequency which is associated with an exponentially growing and spatially oscillating disturbance. Finally, in absolutely unstable flows, a natural wavelength naturally appears as $k_{0,r}$, although several studies have shown that this selection is rarely robust to nonlinear effects [28,29]. Other important nonlinear effects are secondary instabilities: as the emergent pattern progressively saturates, a secondary instability mechanism progressively breaks the periodicity of the pattern. Three classical examples are the pairing or sub-harmonic instability, the sideband or modulational instability [30].

Both the global stability and global resolvent tools naturally extend from spatially invariant flow of finite extent to spatially developing flows. This is particularly relevant in the context of jets ensuing from a nozzle and falling vertically. In the presence of gravity, the liquid jet thins down and is stretched (figure 3*d*), a situation which all of a sudden becomes far more complicated (see [31,32] for recent contributions to that delicate topic).

As a last limitation, we should insist that not all unsteady or pattern-forming flows can be understood from the linear instability point of view. The dynamics of a dripping faucet at sufficiently low flow rate (to allow for a quasi-steady description) provides a daily example. While it is only the limiting case of the jetting phenomenon seen in figure 3*d*, the dripping faucet phenomenon results from the loss of existence of a steady hanging drop solution above a critical volume. The periodic dripping regime results therefore in this situation rather from a singularity in the branch of possible solutions than from the loss of stability of an underlying continuous jet flow solution.

In conclusion, the Rayleigh–Plateau instability and its variants have the peculiar behaviour that (i) there is no control parameter threshold below which the thread is stable, i.e. the instability is unconditional, and that (ii) they are geometrically constrained to one-dimensional patterns, the cut-off wavelength of which is geometrically selected.

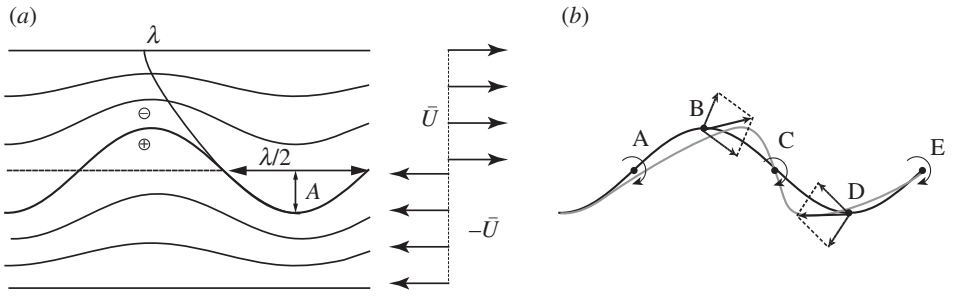

Figure 11. Sketches of Kelvin's (*a*) and Helmholtz's (*b*) interpretations of the instability of a vortex sheet.

(b) Kelvin–Helmholtz instability

The Kelvin–Helmholtz instability concerns the shear flow between two streams with differential velocities. When the fluids are miscible, one talks about a shear layer, but we shall stick to the case of immiscible streams (figure 3*b*).

(i) Physical mechanism and dispersion relation

There are two main interpretations of the development of this instability, both based on a description of the flow appropriate to high Reynolds numbers, where the vorticity is entirely concentrated at the interface, and the flow is irrotational elsewhere. In Kelvin's view (figure 11*a*), the exponential growth of small amplitude waves at the interface results from a Bernoulli pressure correction resulting from this corrugation. Considering a displaced interface, one can show that the potential nature of the flow results in an exponentially damped penetration into both fluids, with a penetration depth scaling as the disturbance wavelength (this is actually the same effect as the so-called skin effect in electromagnetics). Therefore, schematically, the streamlines at a distance further away than λ can be considered undisturbed. This condition imposes the streamtube cross section in the upper fluid to shrink near crests and to widen in the vicinity of troughs and vice versa in the lower fluid. Invoking the conservation of flux in a streamtube, the upper fluid therefore has to accelerate above crests and to decelerate above troughs, while the contrary happens in the lower fluid. From Bernoulli's principle, this results in a pressure imbalance (materialized by $\oplus$ and $\ominus$ in figure 11*a*) which pushes the crests further up and the troughs further down. The loop is closed and exponential growth is ensured.

An alternative interpretation (figure 11*b*), following Helmholtz, is based on the observation that this shear instability results in the focusing of the pre-existing vorticity sheet into a periodic street of concentrated vortices. Considering therefore that a vortex sheet is nothing more than a collection of densely packed point vortices, and coarsening them into only four per period in a thought experiment, their dynamics can be deduced from the interaction with closest neighbours and can easily be shown to result in lateral displacements of the out of symmetry vortices, leading to a progressive steepening and roll-up of the interface.

There is actually a third interpretation which is more suited to a broken line model of the shear layer, which interprets the instability as the interaction of two counter-propagating Rossby waves riding on the facing vorticity discontinuities [33].

The derivation of the dispersion relation assuming that viscous effects can be neglected, that the velocity discontinuity is sharp and that the streams are semi-infinite, is very standard. We provide the dispersion relation here in the slightly more general situation where the fluids are confined by horizontal walls but still infinite in the streamwise direction: the bottom fluid has a depth h_1, velocity $\mathbf{U} = U_1\mathbf{e}_x$ and density ρ_1 while the upper fluid has a depth h_2, velocity U_2 and density ρ_2 and both are submitted to gravity $\mathbf{g} = -g\mathbf{e}_z$. One assumes that the flow is potential in each stream, imposes the impermeability condition on each wall, the linearized kinematic

boundary condition at the interface, as well as the Young–Laplace law, retrieving the pressure from Bernoulli theorem applied separately in each fluid. Assuming a normal mode decomposition $\exp(\mathrm{i}(kx-\omega t))$. The final dispersion relation is written

$$\rho_1\left(U_1-\frac{\omega}{k}\right)^2\coth(kh_1)+\rho_2\left(U_2-\frac{\omega}{k}\right)^2\coth(kh_2)=\left((\rho_1-\rho_2)\frac{g}{k}+\gamma k\right). \tag{3.47}$$

(ii) Unsuccessful application to the wind driven wave formation

This analysis appears as the first attempt to explain the wind–wave formation. Putting $U_1=0$ for the ocean and $U_2=U_{\mathrm{wind}}$ allows one to predict a critical wind speed. The dispersion relation is

$$\omega=\frac{kU_{\mathrm{wind}}\rho_a\pm((\rho_w+\rho_a)(k^3\gamma+(\rho_w-\rho_a)gk)-k^2U_{\mathrm{wind}}^2\rho_a\rho_w)^{1/2}}{\rho_a+\rho_w}. \tag{3.48}$$

This expression makes clear that the shear driven instability will only happen when it overcomes two restoring forces: gravity and surface tension. It yields a critical velocity for the shear instability

$$(U_{\mathrm{wind}}^*)^2>\frac{\rho_w+\rho_a}{\rho_w\rho_a}\left(\gamma k+(\rho_w-\rho_a)\frac{g}{k}\right). \tag{3.49}$$

The minimum is attained for the capillary wavenumber $k_{\mathrm{c}}=\sqrt{(\rho_w-\rho_a)g/\gamma}$ and yields the predicted critical wind velocity for waves to appear

$$(U_{\mathrm{wind}}^*)^2>2\frac{\rho_w+\rho_a}{\rho_w\rho_a}(\gamma g(\rho_w-\rho_a))^{1/2}, \tag{3.50}$$

which for air and water $\gamma=0.07\,\mathrm{N\,m^{-1}}$, $\rho_w=10^3\,\mathrm{kg\,m^{-3}}$ and $\rho_a=1.2\,\mathrm{kg\,m^{-3}}$ yields $U_{\mathrm{wind}}^*=6.6\,\mathrm{m\,s^{-1}}$. Kelvin was already aware of the discrepancy between this predicted critical wind and the commonly observed minimal wind of the order of a couple of metres per second for the first visible ripples on a calm sea. He ascribed this discrepancy to viscous effects, which were not taken into account in the model. Since then, numerous attempts to better predict the onset of wind waves have been proposed, still with limited success. Among the most appealing theories, let us mention that of Miles [34] who demonstrated from a temporal stability analysis of the boundary layer in the air that the neutral gravity wave at the free surface could phase-lock with a vorticity wave in the air if the curvature of the velocity profile is negative at the critical height at which air moves at the same phase velocity as that of the wave, resulting in an exponential growth in time of the wave amplitude.

(iii) Cut-off mechanisms

In the absence of surface tension and density difference, the dispersion relation can be written as

$$\omega=\frac{(U_1+U_2)}{2}k\pm\mathrm{i}\frac{(U_1-U_2)}{2}k. \tag{3.51}$$

The instability travels at the average velocity of the two streams and has a linear growth which is proportional to the shear $|U_1-U_2|$ and to the wavenumber. This unphysical behaviour is relaxed by incorporating a cut-off mechanism at large k. Among the three possible candidates, two are absent in the dispersion relation (3.47), namely a finite shear layer thickness or a finite viscosity, a detailed description of which can be found in [16,35] for the interested reader.

A third cut-off mechanism is however contained in the physical model which has led to (3.47), that is surface tension. For $U_1=-U_2=U$, $\rho_1=\rho_2$ and $h_1\to\infty$, $h_2\to\infty$, the dispersion relation simply becomes

$$\omega=\pm\mathrm{i}\sqrt{k^2U^2-\frac{k^3\gamma}{2\rho}}, \tag{3.52}$$

where the real frequency ω_{r} vanishes, because of the $x\leftrightarrow -x$ symmetry when $U_1=-U_2$, and where a cut-off length $k_{\mathrm{c}}=2\rho U^2/\gamma$ naturally appears, which reflects the balance between the destabilizing shear and the stabilizing surface tension.

(c) Rayleigh–Taylor instability

From the general dispersion described in the previous section, another limit is of particular interest: that of a layer of heavy fluid surmounting a layer of lighter fluid. Like the Rayleigh–Plateau instability, this celebrated Rayleigh–Taylor instability emerges from a fluid situation at rest, but the wavelength is not selected from the geometry of the experiment but rather from the physical properties of the fluid considered and the acceleration field it is submitted to. From equation (3.47), the following dispersion relation is obtained:

$$\omega^2 = \frac{-kg(\rho_1 - \rho_2) + \gamma k^3}{\rho_1 + \rho_2}. \tag{3.53}$$

The underlying physical mechanism could not be simpler. While the upper fluid is prone to be destabilized by gravity, the lower one aims at rising up. In the following, we limit our investigations to the situation of a horizontally infinite layer of liquid under a ceiling. Neglecting the density of air with respect to that of the liquid, as well as viscous and capillary effects, the classical calculation of Rayleigh shows that the growth rate of the instability can be written as

$$\omega_\mathrm{i} = \sqrt{gk\tanh(kh)}. \tag{3.54}$$

This dispersion relation predicts the infinite growth rate of infinitely thin fingers, a situation sometimes called ultraviolet catastrophe. Naturally, this paradox is easily solved by relaxing the absence of surface tension or that of viscous effects, as they both act as stabilizing mechanisms and set a cut-off length. We now turn to their successive analysis.

(i) Regularization by surface tension and wavelength selection

The aforementioned absence of cut-off wavelength can be easily alleviated by restoring surface tension in the problem

$$\omega = \pm\mathrm{i}\sqrt{\left(gk - \frac{\gamma}{\rho}k^3\right)\tanh(kh)}, \tag{3.55}$$

which introduces naturally as cut-off wavenumber $k_\mathrm{c}^2 = \rho g/\gamma$, which is nothing more than the wavenumber associated with the capillary length $l_\mathrm{c} = \sqrt{\gamma/\rho g}$. From a physical standpoint, surface tension prevents the growth of corrugations of the interface that would create too much surface energy. Considering a slightly disturbed interface, the broken hydrostatic balance has be restored by the pressure imbalance between crests and troughs. Considering a trough, which is locally too heavy to be withstood by the air pressure, the negative hydrostatic pressure fluctuation can be compensated by a Laplace pressure contribution, thereby restoring equilibrium. This simple physical explanation explains why a bottle filled with water can be safely turned upside down, when its nozzle has a diameter less than a couple of millimetres. At scales lower than the capillary length l_c, surface tension dominates over gravity and the interface remains flat. In the words of §3a, taking into account the boundary conditions to be imposed at the nozzle wall leads to a quantization of the possible modes $k_n = n\pi/L$. If $k_1 > k_\mathrm{c}$, the flow remains stable.

In the limit of large h, $h \gg l_\mathrm{c}$, the maximum growth rate scales like the typical inviscid growth rate $\omega \sim \pm\mathrm{i}\sqrt{gk_\mathrm{c}}$ while in the small-h limit $h \ll l_\mathrm{c}$, the dispersion relation becomes

$$\omega = \pm\mathrm{i}\sqrt{kh\left(gk - \frac{\gamma}{\rho}k^3\right)}, \tag{3.56}$$

which yields a much lower characteristic growth rate $\omega_\mathrm{i,thin} \sim \pm\mathrm{i}k_\mathrm{c}\sqrt{gh}$. This is one among many examples where confinement has a dampening effect.

(ii) Effect of viscosity for an infinite layer

Viscosity appears in the Rayleigh–Taylor instability also as a stabilizing mechanism. As in the analysis of the Rayleigh–Plateau instability, viscous effects do not change the conditions for

instability of a rest state, but only moderate the rate of growth or decay of disturbances. This is why in such cases the analysis of the stability (or instability) of the inviscid limit can be extremely useful in identifying the conditions for instability, as the inviscid analysis can be much simpler.

However, viscous effects alone are sufficient to progressively damp higher wavenumbers and resolve the infinite growth of infinitely thin fingers in the absence of surface tension. In the absence of a wall, the effect of viscous diffusion can be introduced in a heuristic way by writing a lumped model equation for linearized conservation of vertical momentum which balances inertia $\rho \mathrm{d}v/\mathrm{d}t$, the hydrostatic pressure gradient $\rho g\eta$ and viscous diffusion $\rho\nu k^2 v$ in addition to the kinematic equation $\eta = \mathrm{d}v/\mathrm{d}t$. Introducing the normal mode expansion for the vertical velocity $v\exp(\mathrm{i}(kx-\omega t))$ and for the interface location $\eta\exp(\mathrm{i}(kx-\omega t))$

$$-\mathrm{i}\omega v = gk\eta + \nu k^2 v \tag{3.57}$$

and

$$-\mathrm{i}\omega\eta = v, \tag{3.58}$$

which yields the heuristic dispersion relation

$$\omega^2 + gk - \mathrm{i}\nu k^2\omega = 0. \tag{3.59}$$

The relevance and limitations of this estimate equation have been discussed in detail in [36] and it should be clear that, although it gives the right scalings, it fails in providing the right prefactors (those actually depend on a suitable defined Reynolds number) because it totally ignores the vertical dependence of the velocity field. This equation contains the correct unchanged dependence at large scale where viscosity does not act

$$\omega \sim \mathrm{i}\sqrt{gk} \quad \text{for } k \to 0, \tag{3.60}$$

and the correct scaling at small scale [36,37]

$$\omega \sim \mathrm{i}\frac{g}{\nu k} \quad \text{for } k \to \infty. \tag{3.61}$$

The maximum growth is reached for a wavenumber $k_\mathrm{v} \approx (g/\nu^2)^{1/3}$. Then the typical growth rate becomes $\sigma_\mathrm{v} = \nu(g/\nu^2)^{1/3}$. Viscosity can therefore be safely discarded as long $k_\mathrm{c} < k_\mathrm{v}$, i.e. as the capillary length is larger than the viscous length $l_\mathrm{v} = (\nu^2/g)^{1/3}$.

(iii) Rayleigh–Taylor instability of a thin film

In the presence of a wall, the previous analysis has to be rethought, as viscous effects not only appear in the bulk but also in the vicinity of the wall through the no-slip boundary condition. These lubrication effects can become predominant when the layer is sufficiently thin, as analysed in detail by Limat [38], in which case both viscosity and surface tension have to be taken into account. We will see that the condition for viscous dissipation to be negligible is that the hereafter obtained viscous growth rate $\sigma_{\mathrm{v,thin}}$ (v stands for viscous) is very small with respect to the above found inviscid growth rate $\sigma_{\mathrm{i,thin}}$, which translates into $h^5 \ll l_\mathrm{c}^2 l_\mathrm{v}^3$. Although it is quite classical, let us briefly outline the governing dispersion relation in the viscous thin limit and find the scaling for $\sigma_{\mathrm{v,thin}}$.

The starting point is the Reynolds equation obtained from the kinematic equation and the lubrication approximation

$$\frac{\partial h}{\partial t} = -\frac{\partial}{\partial x}\left(\frac{gh^3}{3\nu}\left(\frac{\mathrm{d}h}{\mathrm{d}x} + l_\mathrm{c}^2\frac{\mathrm{d}\kappa}{\mathrm{d}x}\right)\right), \tag{3.62}$$

where $\kappa = \eta''/(1+\eta'^2)^{3/2}$ is the interface curvature.

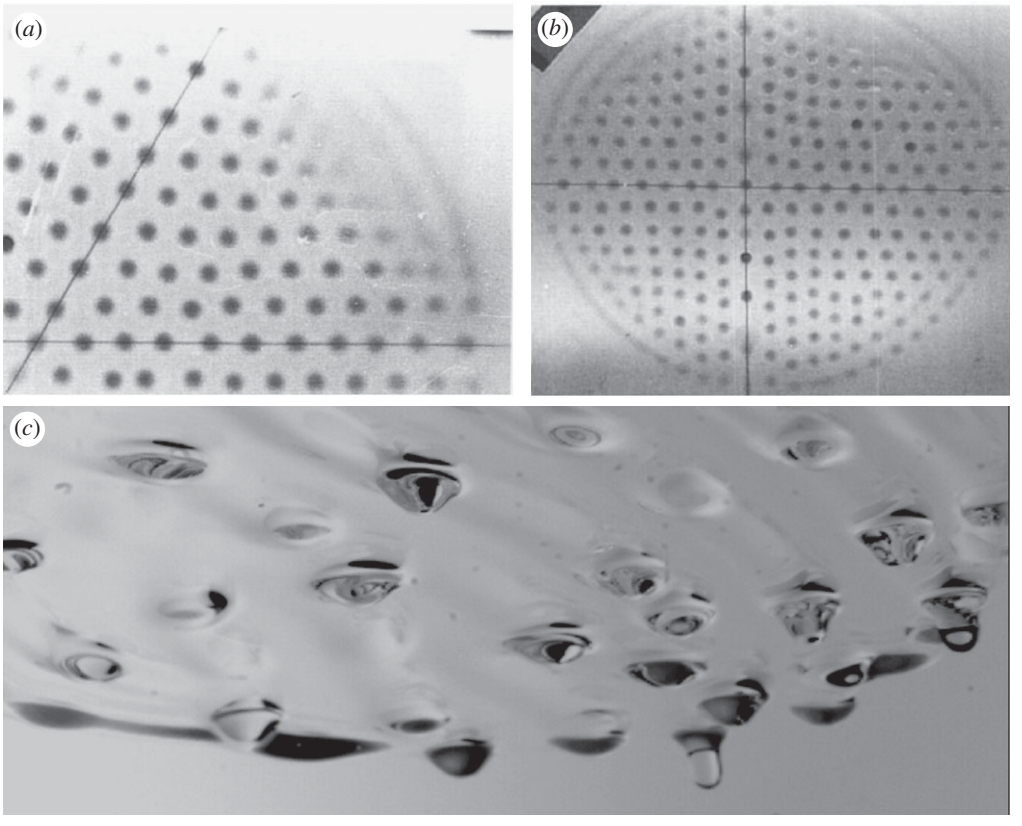

Figure 12. Rayleigh–Taylor instability (from [21,39]). (*a*,*b*) Dripping pattern on a flat substrate. (*c*) Pattern on a slightly inclined plane.

Assuming $\eta = h + \epsilon\eta'(t)$ with $\epsilon \ll 1$ and $\eta'(x,t) \propto \exp(\mathrm{i}(kx - \omega t))$, the following dispersion relation is obtained:

$$\omega = \mathrm{i}\frac{gh_0^3}{3l_c^2\nu}(k^2l_c^2 - k^4l_c^4). \tag{3.63}$$

Observe the exact similarity with the dispersion relation for the Rayleigh–Plateau instability on a fibre (3.23). Again this instability is unconditional, at least at the linear level. It has no critical threshold. Experimentally, the wavelength selection very well obeys the most unstable wavelength [39]. However, a diversity of patterns are observed. While the hexagonal pattern appears as the most robust away from the boundaries, square patterns can also be easily obtained by adding defects or by shaping the lateral boundaries (figure 12*a*,*b*). Although the analysis has been conducted here in the two-dimensional (x,z) plane, while in experiments there exists another transverse direction y, the perfect isotropy of the physical problem in the (x,y) plane translates easily in the dispersion relation by replacing k by $|\mathbf{k}|$, where $\mathbf{k} = k_x\mathbf{e}_x + k_y\mathbf{e}_y$. This dispersion relation then does not allow one to distinguish the growth of different patterns and the pattern formation has to be analysed nonlinearly. The absence of threshold causes the analytical treatment of the nonlinear saturation process to be very difficult (attempts in [39,40]). It is therefore hard to predict the resulting two-dimensional pattern for extended substrates. Heuristic amplitude equations have been proposed in [39], which suggest the dominance of the hexagonal pattern over rolls and squares, but as acknowledged by the authors themselves, their analysis remains quite qualitative.

In view of the evident applicative interest of suppressing dripping from a ceiling, effects of drying through solvent evaporation (evaporation in itself can already stabilize the flow) or curing

through cross-linking of polymers as well as Marangoni effects have been analysed, as more practical complement to active control strategies, in closed loop and open loop. More recently, the effect of tilting the ceiling has been studied [21]. This introduces a mean advection and raises the question of the absolute or convective nature of the instability as well as open questions on the pattern selection process (figure 12*c*).

(d) Faraday instability

(i) Physical mechanism: a parametric instability

The Faraday instability appears when a bath of liquid is vibrated vertically. As reviewed for instance by Fauve [30], the physical mechanism results from the parametric instability of the neutral capillary-gravity waves that oscillate in the liquid bath, referred to as sloshing modes. The dispersion relation pertaining to capillary-gravity waves in a container of finite depth is the exact counterpart of the Rayleigh–Taylor unstable modes (3.55), provided the two purely real eigenvalues (one being unstable and the other one damped) are replaced by two purely imaginary eigenvalues (both propagating in opposite directions). The unavoidable effect of damping is first neglected.

The parametric excitation of these waves by the vertical vibration of the vessel bears a strong similarity to a vertical vibrated pendulum [41,42]. The amplitude η of the normal mode decomposition of the perturbed interface obeys indeed the following equation:

$$\ddot{\eta} + k\tanh(kh)\left(g + d\omega_{\mathrm{f}}^2\cos(\omega_{\mathrm{f}}t) + \frac{\gamma}{\rho}k^2\right)\eta = 0, \tag{3.64}$$

where k is the wavenumber, h the fluid depth and d the oscillation amplitude. For $d = 0$, the unforced natural frequency is recovered

$$\omega_0^2 = k\tanh(kh)\left(g + \frac{\gamma}{\rho}k^2\right). \tag{3.65}$$

The numerical and analytical manipulation of equation (3.64) is made easier by considering ω_0 and f as variables while considering ω_{f} as fixed and rescaling time with ω_{f}^{-1}, which yields a Mathieu-like equation

$$\ddot{\eta} + (a^2 + 2b\cos(t))\eta = 0, \tag{3.66}$$

where $a^2 = \omega_0^2/\omega_{\mathrm{f}}^2$ and $b = \mathrm{d}\omega_0^2/2(g + \gamma k^2/\rho)$. The general theory for linear dynamical systems with periodic coefficients is known as Floquet theory. It predicts the existence of both stable and unstable solutions as a function of a and b, as seen in figure 13*a*. Inside the stability tongues the solutions are found to remain bounded (periodic or quasi-periodic), while outside these tongues, there exists at least one unstable solution. Observe that this result cannot be naively predicted by requiring, in a quasi-static sense, that the instantaneous eigenfrequency remains real, i.e. that $b < a^2/2$.

Let us first consider the limit $b \ll 1$, that is the forcing has a small amplitude. Formally, we shall write $b = \epsilon b_1$ and look for a solution of the form $\eta(t) = \eta_0(t) + \epsilon\eta_1(t) + \epsilon^2\eta_2(t) + \cdots$. The equations can be separated at each order

$$\ddot{\eta}_0 + a^2\eta_0 = 0, \tag{3.67}$$

$$\ddot{\eta}_1 + a^2\eta_1 = -2b_1\cos(t)\eta_0 \tag{3.68}$$

and

$$\ddot{\eta}_2 + a^2\eta_2 = -2b_1\cos(t)\eta_1. \tag{3.69}$$

The solution at zero order

$$\eta_0 = A\exp(\mathrm{i}at) + \text{c.c.} \tag{3.70}$$

is purely oscillating and allows one to write at next order

$$\ddot{\eta}_1 + a^2\eta_1 = -b_1((A\exp(\mathrm{i}(a+1)t) + A\exp(\mathrm{i}(a-1)t)) + \text{c.c.}). \tag{3.71}$$

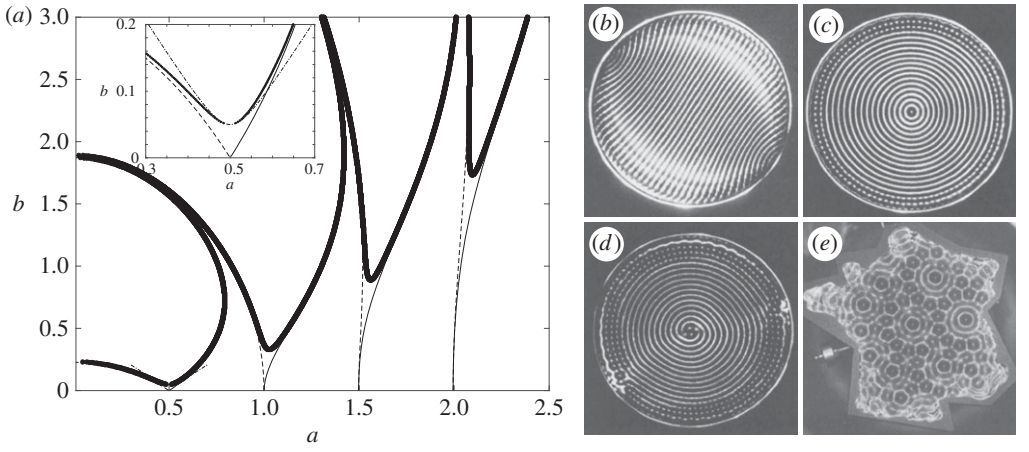

Figure 13. Faraday instability; (*a*) instability tongues of a canonical parametric instability without (continuous lines) and with (dots) damping $\lambda/\omega_f = 0.05$. Instability appears inside the tongues. The asymptotic expression (3.81) is also included as thin dash-dotted line (better visible in the inset close to $a = 0.5$). Patterns include (*b*) lines, (*c*) circles and (*d*) quasi-patterns whose nature is independent of the sidewall geometry (from [43]).

The particular solution of this equation will grow algebraically in time if the r.h.s. resonates

$$a \pm 1 = \pm a, \tag{3.72}$$

i.e. if $a = \pm\frac{1}{2}$. Thus, provided $a \neq \frac{1}{2}$, the solutions for η_1 remain bounded for all time. A similar reasoning can be held at successive orders, yielding recursive resonances at $a = \pm n/2$. This illustrates that the solutions from which the Mathieu tongues emanate have a periodicity π/n and all share 4π as common period. This property can be shown rigorously by Floquet theory and is of paramount importance in the numerical code that has enabled the plot in figure 13. In the latter, one interprets equation (3.66) as an eigenvalue problem: for a given value of b, and π-periodic η functions, find all values of a^2 which are eigenvalues of

$$\ddot{\eta} + 2b\cos(t)\eta = -a^2\eta. \tag{3.73}$$

Coming back to the physical quantities, this shows the existence of unstable solutions in the limit of small parametric forcing amplitude for forcing frequencies $\omega_f = 2\omega_0/n$ for $n \in \mathbb{N}^+$. Sloshing waves are therefore parametrically excited by the first harmonic $2\omega_0$, the sloshing frequency itself ω_0 and by a series of subharmonic frequencies $2\omega_0/3$, $\omega_0/2$, etc. One should also remember that there is a countable infinity of sloshing modes in the vessel (indexed by $m \in \mathbb{N}^+$) as a consequence of the quantization by the boundary conditions, which implies that altogether parametric resonances will exist for $\omega_f = 2\omega_0^m/n$. However, the presence of damping will be seen in next subsection to quantitatively affect these modes differently.

(ii) Role of damping

The analysis of the effect of viscosity on the damping rate of the sloshing mode is even more difficult than the analysis proposed in §3c, as the consequence of the necessary presence of lateral walls. Not only do they produce a quantization of the sloshing frequencies, but they also create an additional and, often dominant, source of damping, resulting from Stokes layers on the wall [44]. Additionally, the dissipation at the contact line remains an unsettled issue [45–47]. For all these reasons, it is fair to introduce damping in a phenomenological way, introducing an additional term in equation (3.64) $2\lambda(k)(\mathrm{d}\eta/\mathrm{d}t)$ and assume that $\lambda(k)$ increases with k, because oscillations at smaller scale dissipate more. This effect highlights the relevance of the fundamental mode at largest scale at natural frequency ω_0^1, the mode that satisfies the boundary conditions with fewer

possible oscillations. The damping term translates in the non-dimensional equation (3.66) into

$$\ddot{\eta} + 2c\dot{\eta} + (a^2 + 2b\cos(t))\eta = 0, \tag{3.74}$$

where $c = \lambda(k)/\omega_f$.

Let us therefore now examine the role of damping and nonlinearity in the resonance mechanism at the lowest sloshing frequency ω_0^1 by a multiple scale expansion. Although the approach can be generalized to other resonances, we shall focus on the first resonance of the first mode $\omega_f = 2\omega_0^1$ (i.e. $a = \frac{1}{2}$) and set $a = \frac{1}{2} + \epsilon a_1$ and $c = \epsilon c_1$. Additionally, in order to properly investigate the secular growths, let us introduce a slow time scale $T = \epsilon t$.

At zero order, the equation is unchanged and the solutions very similar, although the amplitude now depends slowly on time

$$u_0 = \frac{A(T)\exp(\mathrm{i}t)}{2} + \text{c.c.} \tag{3.75}$$

At next order, several new terms appear

$$\ddot{u}_1 + \frac{1}{4}u_1 + \text{c.c.} = -2\frac{\partial^2 u_0}{\partial t \partial T} - a_1 u_0 - 2c_1\frac{\partial u_0}{\partial t} - 2b_1\cos(t)u_0. \tag{3.76}$$

In order to avoid the growth of secular terms, the forcing term resonating with $\exp(\mathrm{i}t/2)$ should be cancelled which yields the following amplitude equation:

$$\frac{\mathrm{d}A}{\mathrm{d}T} - \mathrm{i}a_1 A + c_1 A - \mathrm{i}b_1 A^* = 0. \tag{3.77}$$

Decomposing A into its real and imaginary parts $A = X + \mathrm{i}Y$ yields

$$\frac{\mathrm{d}X}{\mathrm{d}T} + a_1 Y + c_1 X - b_1 Y = 0 \tag{3.78}$$

and

$$\frac{\mathrm{d}Y}{\mathrm{d}T} - a_1 X + c_1 Y - b_1 X = 0. \tag{3.79}$$

This is a genuine oscillator equation with eigenvalues

$$s = -c_1 \pm \sqrt{(b_1^2 - a_1^2)}. \tag{3.80}$$

The condition for instability is therefore

$$b_1^2 > a_1^2 + c_1^2. \tag{3.81}$$

The instability tongue therefore does not emerge directly at vanishing forcing amplitude; it requires a minimal forcing amplitude to overcome the damping. This relation is also plotted together in figure 13. This figure also reveals that the minimum forcing amplitude which defines the bottom of the resonance tongue increases more than linearly with the resonance number n. As it also increases with the wavevector, it shall be clear that the first parametric instability to appear when the amplitude is progressively increased is the sub-harmonic of the fundamental spatial mode $\omega_f = \omega_0^1$.

(iii) Pattern selection

Faraday instability has been used as a prototype instability for several studies in pattern formation, including roll/square/hexagon transitions by Fauve and co-workers (see [30] for a review) as it enabled refined studies by easily varying two control parameters, the forcing amplitude and frequency. Figure 13 displays a certain number of possible patterns found by vibrating a thin bath of liquid. To elucidate the pattern selection, the first step, still considering a single wavevector orientation, is to derive an amplitude equation generalizing the weakly

nonlinear analysis described in the previous subsection to include nonlinearties in the fluid equations,

$$\frac{\mathrm{d}A}{\mathrm{d}T} - \mathrm{i}a_1 A + c_1 A - \mathrm{i}b_1 A^* + \nu_1 |A|^2 A = 0, \tag{3.82}$$

where ν_1 was determined experimentally [42]. This equation describes the nonlinear saturation of so-called rolls.

The second step is to consider the interaction of different wavevector directions, in order to understand the governing nonlinear pattern selection processes. In the absence of in-plane boundary conditions, a square pattern needs for instance the superimposition of two vectors, say along $\mathbf{e}_x$ and $\mathbf{e}_y$ as well as their associated amplitudes A and B. For hexagons, three modes with wavevectors forming an equilateral triangle need to be added together. The resulting amplitude equations are also often deduced by symmetry considerations and the coefficients tuned by experiments. They enable a subsequent pattern stability analysis. It can be seen for instance that the concentric standing wave pattern shown in figure 13*c* is unstable with respect to modulations perpendicular to the wave crests in favour of a stable square stationary standing wave pattern (figure 13*b*). This general amplitude equation approach has allowed [42] to even study the formation of quasi-crystal patterns using a double frequency forcing.

(e) Rayleigh–Bénard–Marangoni

The history of Rayleigh–Bénard–Marangoni convection is noteworthy, as the seminal experiments by Bénard were undertaken in conditions where the buoyancy effects at the heart of the study of Rayleigh were overshadowed by Marangoni effects that were taken into account only much later [48]. The richness of patterns formed in this flow configuration has led to a myriad of studies and some observed patterns are gathered in figure 15. When the flow is driven even further away from threshold, a series of bifurcations lead to chaos and turbulence through different possible routes that have attracted much attention. We here focus on the primary instability and first derive the dispersion relations pertaining to buoyancy and Marangoni separately, so as to discuss their competition. We then briefly discuss what tools are required to analyse the pattern formation in such two-dimensional extended systems.

(i) Rayleigh–Bénard

In the absence of Marangoni effect, this instability is called Rayleigh–Bénard. It is driven by the buoyancy force. The fluid heated from below moves up because it is lighter than its environment. To be more quantitative, let us consider a layer of depth d of liquid of density ρ, kinematic viscosity ν, dynamic viscosity $\mu = \rho\nu$ in a gravitational field $\mathbf{g} = -g\mathbf{e}_z$. We follow Boussinesq's hypothesis and assume that ρ, μ (and therefore ν) are temperature independent except in the buoyancy term. Under these assumptions, the flow remains incompressible, but is submitted to a locally varying buoyancy force. The density is assumed to vary linearly with temperature $\rho = \rho^{(b)} - \alpha(T - T^{(b)})$ and surface tension. The base temperature profile (the base flow) is given by

$$T = T^{(b)} + \frac{T^{(a)} - T^{(b)}}{d} z, \tag{3.83}$$

where $z = 0$ is set at the bottom plate. The heat diffusivity of the fluid is designated by κ.

The following non-dimensionalization is used: d as length, d^2/κ as time (and therefore $d\kappa$ as velocity), $\rho\kappa^2/d^2$ as pressure and $\kappa\nu/\alpha g d^3$ as temperature gauges. After some manipulations, the linearized equations around the base flow can be formulated for two unknowns only (the vertical velocity perturbation u_z' and the temperature fluctuation T')

$$\frac{\partial \Delta u_z'}{\partial t} = Pr\Delta^2 u_z' + Pr\Delta_\parallel T' \tag{3.84}$$

and

$$\frac{\partial T'}{\partial t} = Ra u_z' + \Delta T', \tag{3.85}$$

Table 3. Critical parameters for Rayleigh–Bénard convection.

BC velocity	BC temperature	critical Rayleigh number	critical wavenumber
rigid/rigid	fixed/fixed	1708	3.16
free/free	fixed/fixed	658	2.22
rigid/free	fixed/fixed	1101	2.68
rigid/free	fixed/insulating	669	2.02

where $\Delta = \partial^2/\partial x^2 + \partial^2/\partial y^2 + \partial^2/\partial z^2$ and $\Delta_\parallel = \partial^2/\partial x^2 + \partial^2/\partial y^2$ and where $Ra = \alpha g d^3 (T^{(b)} - T^{(a)})/\kappa\nu$ and $Pr = \nu/\kappa$.

A normal mode decomposition exploiting the invariance of the base flow with x, y and t $\exp(\mathrm{i}(k_x x + k_y y - \omega t))$ is then introduced with k_x and k_y the horizontal wavenumbers and ω the frequency. Noting $k^2 = k_x^2 + k_y^2$, $D = \mathrm{d}/\mathrm{d}z$ and using the hat $\hat{(\,)}$ to designate z-dependent variables, this yields

$$-\mathrm{i}\omega(D^2 - k^2)\hat{u}_z = Pr(D^4 - 2k^2D^2 + k^4)\hat{u}_z - Prk^2\hat{T} \tag{3.86}$$

and

$$-\mathrm{i}\omega\hat{T} = Ra\hat{u}_z + (D^2 - k^2)\hat{T}. \tag{3.87}$$

We consider a free surface at the top boundary but a solid wall at the bottom. We impose no slip at the bottom wall and free-stress at the upper one. The boundary conditions for the velocity and temperature are

$$\left.\frac{\mathrm{d}\hat{u}_z}{\mathrm{d}z}\right|_{z=0} = \left.\frac{\mathrm{d}^2\hat{u}_z}{\mathrm{d}z}\right|_{z=1} = \hat{u}_z|_{z=0,1} = \left.\frac{\mathrm{d}\hat{T}}{\mathrm{d}z}\right|_{z=1} = \hat{T}|_{z=0}. \tag{3.88}$$

In the particular case of free/free boundary conditions as studied by Rayleigh (an experimental situation achieved much later than Rayleigh's calculation), this one-dimensional eigenvalue problem can be solved analytically through a harmonic sinus expansion. In all the other cases, numerical approaches are necessary. Among those, spectral methods are preferred as certain choices of basis yield a rapid convergence, but for the purpose of illustration, we have implemented simple second-order finite differences to solve the problem. We find that there is a critical Ra parameter $Ra_\mathrm{c} = 669$ above which a finite range of wavenumbers becomes unstable centred around the critical $k_\mathrm{c} = 2.02$ (figure 14*a*).

As described in table 3, the critical Rayleigh number and wavenumber both depend on the choice of boundary conditions. It is probably the right place to mention that these critical values can be obtained by applying the so-called principle of exchange of instability. The latter stipulates that when a flow bifurcates from a rest situation, then it often does so by an eigenvalue that goes through $\omega = 0$ at the critical point. This transforms the eigenvalue problem into a pure set of coupled linear ODEs which can often be solved analytically. This principle however excludes Hopf bifurcations, where eigenvalues have a finite real part ω_r at the critical control parameter value, and has to be derived on a case-to-case basis. It should therefore be manipulated with extreme care.

(ii) Bénard–Marangoni

We now turn to the pure Bénard–Marangoni instability, neglecting the Archimedes force and taking ρ constant. However, the surface tension γ is now taken into account, still ignoring surface deformations though. The inhomogeneous surface temperature creates strong surface tension variations which in turn create Marangoni stresses, according to the tangential stress discontinuity $\mathbf{t}\cdot\sigma\mathbf{n} = \nabla\gamma\cdot\mathbf{t}$, where σ designates the stress tensor $\sigma = -pI + \mu(\nabla\mathbf{u} + \nabla\mathbf{u}^t)$. We further assume that the surface tension γ varies linearly with temperature, according to $\gamma = \gamma^a + \beta(T - T^{(a)})$.

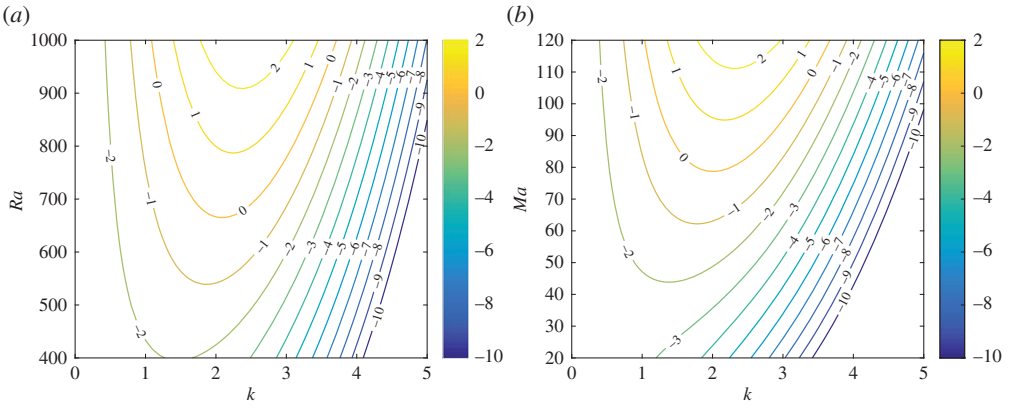

Figure 14. (*a*) Isocontours of growth rate in the *k*–*Ra* plane for a buoyancy driven convection with a bottom wall at constant temperature and a free insulating surface. (*b*) Isocontours of growth rate in the *k*–*Ma* plane for a Marangoni driven convection with the same boundary conditions. (Online version in colour.)

Therefore, *Ra* should be set to zero in equation (3.86) but the boundary condition should be replaced from free stress to Marangoni stresses, which results in a surface motion that pulls from the high surface tension region towards the low surface tension region, therefore from the cold to the hot region. Mathematically, the Marangoni condition is written

$$\mu\left(\frac{\partial u_x}{\partial z}+\frac{\partial u_z}{\partial x}\right)\bigg|_{z=1}=\beta\frac{\partial T}{\partial x}\bigg|_{z=1} \tag{3.89}$$

and

$$\mu\left(\frac{\partial u_y}{\partial z}+\frac{\partial u_z}{\partial y}\right)\bigg|_{z=1}=\beta\frac{\partial T}{\partial y}\bigg|_{z=1}. \tag{3.90}$$

Interestingly, this condition is linear and directly translates to the perturbation expansion.

The non-dimensional Marangoni number *Ma* compares the driving force to the viscous friction force and is written

$$Ma=\frac{\beta(T^{(b)}-T^{(a)})d}{\mu\kappa}. \tag{3.91}$$

Using incompressibility and continuity, a compact equation is obtained for the vertical velocity at the interface, which after the normal mode expansion becomes

$$-\frac{\mathrm{d}^2\hat{u}_z}{\mathrm{d}z^2}\bigg|_{z=1}=-Mak^2\hat{T}. \tag{3.92}$$

Solving this problem numerically (the critical Marangoni number and wavenumber can be obtained analytically invoking the principle of exchange of instability), one finds $Ma_c=80$ and $k_c=1.99$ (figure 14*b*).

Suppose now that the temperature gradient is fixed, then the critical Rayleigh number scales as d^4, while the critical Marangoni number scales only as d^2. We therefore anticipate that if the layer is sufficiently thin, then the Marangoni instability is likely to appear before the Rayleigh–Bénard one. Pearson [48] has shown that Bénard's experiments were run in a range where the onset of the instability resulted from Marangoni effects.

(iii) Pattern selection in two-dimensional systems

Several examples of patterns observed above threshold are reproduced in figure 15, demonstrating that, together with the Rayleigh–Taylor instability of a thin layer (see §3c) and the Faraday instability (see §3d), the Rayleigh–Bénard–Marangoni instability provides a

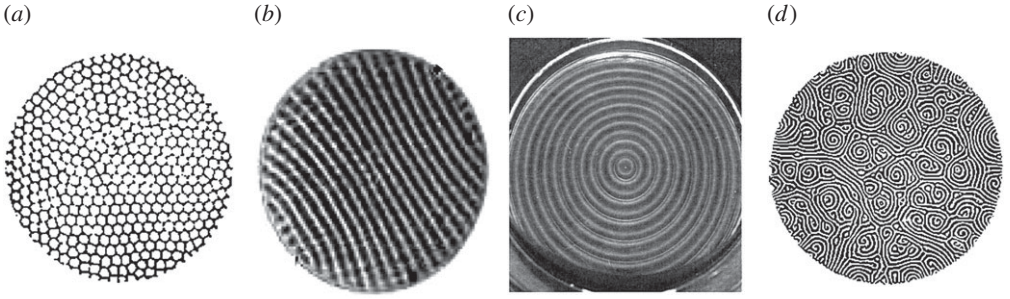

Figure 15. Several patterns in convection. (*a*) Bénard's initial experiment, (*b*) rolls found by Croquette, circular patterns by Koschmieder (*c*), and serptenine patterns by Ahlers (*d*). See [49] for full references.

vast diversity of patterns. As seen in the associated dispersion relations, this results from the isotropy of the dispersion relation with respect to the wavenumber direction, as only its norm k enters the stability problem. There is therefore a pattern degeneracy that results from the linear approximation; indeed, any superposition of normal modes is also a solution. The pattern selection can therefore only result from nonlinear or boundary condition effects. For example, the description of a hexagonal pattern requires three amplitudes A_n, with $n \in \{1,2,3\}$, one for each of the three wavevectors $\mathbf{k}_n$ forming an equilateral triangle $\mathbf{k}_1 + \mathbf{k}_2 + \mathbf{k}_3 = 0$ and of norm $|\mathbf{k}_n| = k_c$, according to

$$u_z'(x,y,z,t) = \hat{u}_z \sum_{n\in 1,2,3} A_n(T) \exp(\mathrm{i}(\mathbf{k}_n.\mathbf{x})), \tag{3.93}$$

where $\mathbf{x} = (x,y)$. The resulting coupled set of amplitude equations is written in compact form for the cyclic permutations of (l,m,n)

$$\frac{\partial A_l}{\partial T} = \sigma A_l + \kappa A_m A_n + (\nu |A_l|^2 + \mu(|A_m|^2 + |A_n|^2))A_l, \tag{3.94}$$

where quadratic and cubic terms have been gathered at the same order (see [30] for a discussion on the validity of this hypothesis and on the several coupling coefficients κ, ν and μ introduced). These equations and their counterparts for different patterns can be used to study pattern stability and selection. Whether rolls, squares or hexagons are predominant was shown to critically depend on the boundary conditions. As reviewed by [30], the studies on Rayleigh–Bénard convection with symmetric boundary conditions all concluded for the dominance of roll patterns. However, when the symmetry is broken, as in the two situations considered in this section, hexagons are preferred. Observe that those appearing in thin convecting layer produced by the Marangoni effect have fluid sinking in the centre of the cells, while in thicker layers, the Rayleigh mechanism produces hexagons with fluid sinking at the cell edges [49].

An even more powerful description than this set of coupled amplitude equations are coupled envelope equations, which generalize amplitude equations to slow modulations in space and time. They are widely used in the study of pattern selection in spatially extended systems, and have therefore received extended attention and dedicated review papers and our objective is here only to provide a brief overview of the overarching principles. Considering for instance the Rayleigh–Bénard instabilities, the existence of a critical parameter allows for their rigorous derivation, as exemplified now for rolls aligned in the y direction (therefore with wavevector in the x direction). Considering a small departure from threshold $Ra = Ra_c + \epsilon$, such that the frequency is written as $\omega = \epsilon\Omega$ and the wavenumber $\mathbf{k} = k^c\mathbf{e}_x + \epsilon K_x + \sqrt{\epsilon}K_y$, it is natural to introduce slow space and times scales $X = \sqrt{\epsilon}x$, $Y = \sqrt{\epsilon}y$ and $T = \epsilon t$ and to approximate the flow field as the product of a slowly evolving envelope and the eigenmode prevailing at threshold $\hat{u}_z^c(z)$

$$u_z(x,y,z,t) = \sqrt{\epsilon}A(X,Y,T)\hat{u}_z^c(z)\exp(ik^c x). \tag{3.95}$$

Imposing the non-resonance condition results in the amplitude equation

$$\frac{\mathrm{d}A}{\mathrm{d}T} = \Omega A - \nu|A|^2 A + \kappa\left(\frac{\mathrm{d}}{\mathrm{d}X} - \frac{\mathrm{i}}{2k_\mathrm{c}}\frac{\mathrm{d}^2}{\mathrm{d}Y^2}\right)^2 A, \tag{3.96}$$

which governs the modulation in space and time of the roll pattern and where the coefficients ν and κ can be obtained analytically [50,51]. Similar amplitude equations can be obtained for other patterns and help in determining their stability.

For the influence on pattern selection of advection, the reader is referred to the studies of [52, 53] on Rayleigh–Bénard–Poiseuille flow, among others.

(f) Saffman–Taylor instability

(i) Physical mechanism and dispersion relation

Viscous fingering, also called Saffman–Taylor instability, is considered as an archetype of pattern forming instability, as reviewed for instance in [54]. It has also been widely studied in the context of industrial research, such as petroleum extraction in particular. The phenomenon belongs to the broad family of instabilities of growth in Laplacian fields, which includes solidification, aggregation, etc. It was first studied by Saffman & Taylor in 1958 [55], who investigated the formation of fingers upon injection of a fluid into a shallow rectangular channel (also called a Hele-Shaw cell), filled with a different immiscible and more viscous fluid.

At leading order, the pressure driven flow in the cell has a Poiseuille profile, and the situation can be described by a depth-averaged two-dimensional potential flow model, where the mean in-plane velocity $\bar{\mathbf{u}}$ is proportional to the pressure gradient in each fluid, with the proportionality constant scaling inversely with the viscosity and with the cell gap square, according to the so-called Hele-Shaw approximation

$$\bar{\mathbf{u}}_i = -\frac{b^2}{12\mu_i}\nabla p_i, \tag{3.97}$$

where $i = 1, 2$ indicates the two immiscible fluids. This equation is nothing more than Darcy's law, which governs the dynamics of flows in porous media. A Hele-Shaw cell thus can be seen as a model system for a porous medium with permeability $K = \frac{b^2}{12\mu}$. The thinner the cell and the more viscous the fluid, the less permeable is the cell. The nonlinear interface conditions are

$$\frac{\partial \eta}{\partial t} + \bar{\mathbf{u}}_i.\mathbf{e}_y \frac{\partial \eta}{\partial y} = \bar{\mathbf{u}}_i.\mathbf{e}_x \quad \text{for } i = 1, 2 \tag{3.98}$$

and

$$p_1 - p_2 = \gamma \frac{\partial^2\eta/\partial y^2}{(1 + \partial\eta/\partial y^2)^{3/2}}. \tag{3.99}$$

As a consequence of the incompressibility of the depth-averaged flow, the pressure is a Laplacian field

$$\Delta p = 0. \tag{3.100}$$

This equation provides a first rationale for this instability, best described when the invading fluid is inviscid and therefore assumed at constant pressure. As illustrated in figure 16*a* by the isocontours of the the pressure field, any emerging finger enhances the pressure gradients acting in the tip region, in close similarity to the tip effect in electrostatics. Because the interface moves with a velocity proportional to the pressure gradient, the feedback loop is closed. Any minute initial displacement will turn unstable, as it increases the pressure gradient and further accelerates a protruding finger, which in turn becomes steeper and steeper as it continues to develop. This instability is damped by surface tension, which acts to minimize the interface area and opposes the formation of curved fingers. One key parameter that determines the number and shape of fingers is therefore the ratio between viscous effects, represented by the product of the interface

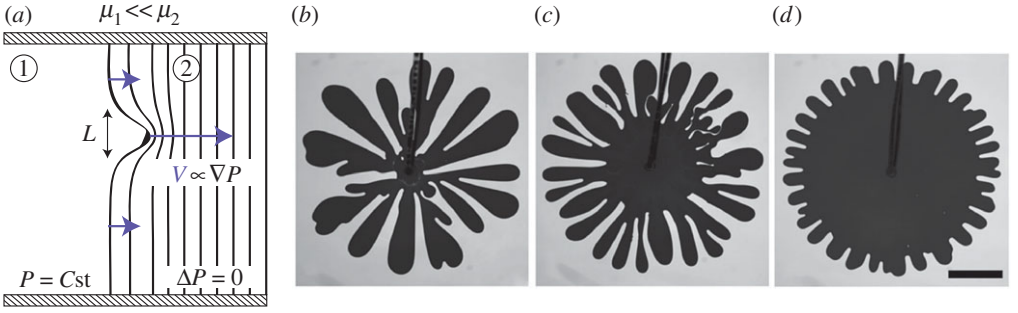

Figure 16. (*a–d*) Saffman–Taylor mechanism and pattern selection in radial injection as a function of the viscosity ratio (from [56]). (Online version in colour.)

velocity U and the viscosity difference $\mu_1 - \mu_2$, against capillary effects represented by the surface tension γ. This ratio is called the capillary number $Ca = (\mu_1 - \mu_2)U/\gamma$.

A somewhat similar interpretation is well summarized in [57], according to which the Saffman–Taylor instability results from the difference in permeability between the two fluids. We see from Darcy's law that a fluid with a large K moves faster under the action of a given pressure gradient than a fluid with a smaller K. Let us take $U > 0$ such that both fluids (fluid 1 to the left of the interface and fluid 2 to the right) move to the right. Fluid 2 at the right has a smaller value of permeability (it is more viscous) and hence the pressure gradient needed to move it is larger than the pressure gradient in fluid 1 (at the left) where the value of the permeability is larger (it is less viscous). Suppose a sinusoidal perturbation of the interface across the nominally flat vertical interface. Where the interface penetrates rightward, the left fluid momentarily finds itself in a region where the pressure gradient is larger than the one that is needed to move at velocity U. This tends therefore to make this region, which is already in advance with respect to the remaining fluid, move faster thus accentuating the amplitude of the perturbation. Conversely, where the interface is momentarily lagging behind (the fluid to the right has penetrated to the left of the nominally flat interface), the local pressure gradient is lower than that needed to travel at velocity U. Therefore the fluid slows down, which further amplifies the perturbation. While this 'hand-waving' description of the instability is oversimplified, it reflects the ingredients needed to derive the dispersion relation, as detailed below.

Let us proceed to the stability analysis of a plane front propagating at constant velocity $U\mathbf{e}_x$. The base pressure field is given by

$$P_i = \frac{U}{K_i}(x - Ut), \tag{3.101}$$

such that the pressure is continuous on the undisturbed interface $\eta = Ut$. Next a perturbation expansion method is used with $p = P + \epsilon p'$, $\mathbf{u} = U\mathbf{e}_x + \epsilon \mathbf{u}'$ and $\eta = Ut + \epsilon \eta'$, where $\epsilon \ll 1$. The linearization of the equations is trivial except at the interface

$$\Delta p_i = 0, \quad p_1' - p_2' = \gamma \frac{\partial^2 \eta'}{\partial y^2} \tag{3.102}$$

and

$$\bar{\mathbf{u}}_i' = -\frac{b^2}{12\mu_i}\nabla p_i', \quad \frac{\partial \eta'}{\partial t} = \bar{\mathbf{u}}_i' . \mathbf{e}_x. \tag{3.103}$$

Considering the independent fate of each wavenumber k chosen to be real positive in the y direction (without loss of generality), it is natural to look for a normal mode expansion $p_i = \hat{p}_i \exp(\mathrm{i}(ky - \omega t))$ and $\eta' = C \exp(\mathrm{i}(ky - \omega t)$ suggested by the invariance of the base flow solution

with respect to y. Imposing far field boundary conditions in each fluid yields

$$\hat{p_1} = A_1 \exp(kx), \quad \hat{p_2} = A_2 \exp(-kx), \tag{3.104}$$

which readily yields the final dispersion

$$\omega = \mathrm{i}\left(\frac{\mu_1 - \mu_2}{\mu_1 + \mu_2} Uk - \gamma \frac{b^2}{12} \frac{k^3}{\mu_1 + \mu_2}\right). \tag{3.105}$$

This dispersion relation displays a cut-off at $k_c = (2/b)\sqrt{(\mu_1 - \mu_2)U/\gamma}$, which highlights the key role of the capillary number defined earlier in the mitigation by surface tension of the viscous fingering mechanism.

(ii) Radial geometry and three-dimensional effects

While this linear stability analysis succeeded in capturing the essence of the instability mechanism, it was soon recognized that it failed in providing a wavelength-selection mechanism. In linear channels, the finger width was found to scale with the channel width as a result of a nonlinear process, with surface tension acting as selection mechanism, however small it may be. This puzzle was solved by three different groups in the same year, using involved asymptotic approaches. The stability of the nonlinear fingers with respect to two idiomatic secondary instabilities, tip-splitting and side-branching, has also been analysed.

The pattern selection mechanism predicting the number of fingers in radial injection does not appear as easier. While a generalized dispersion relation can be derived in circular geometry, it fails in predicting the correct finger number. The agreement can be partially improved by considering a more refined model than the Darcy equations [58], although a more accurate treatment is likely to require a full or lumped description of the out of plane meniscus region.

The branch-like structure appearing in radial growth results from both the above mentioned secondary instability mechanisms, tip-splitting and side-branching. However, recent studies have revealed the important role of the viscosity ratio at low surface tension, as it can induce a transition from the classical regime dominated by long highly branched fractal fingers to one dominated by blunt stable structures characteristic of proportionate growth [56]. Typical examples are reported in figure 16.

(g) Contact line fingering instabilities

(i) The capillary ridge instability

When a liquid mass is flowing down a partially wetting inclined plate, the interface breaks into fingers, as first experimentally found by Huppert [59] from which figure 17*a* is reproduced. Very familiar examples are candle wax drips or paint fingers. As further analysed from the instability point of view in [60–62] among many others, the mechanism for the instability involves a subtle interplay between the fluid far from the front, where surface tension is irrelevant, and the fluid near the contact line, where surface tension dominates. This interplay results in the existence, slightly ahead of the contact line, of a thick fluid bump or capillary ridge (figure 17*b*, inset), that is responsible for the linear instability. Therefore, in order to properly describe this capillary ridge instability the base flow has first to be determined. It is the first instance in this review where the base flow is not given and has to be computed numerically or asymptotically. This determination does not only require one to solve a nonlinear fluid dynamics problem, it also poses a severe modelling issue, as the contact line dynamics has to be modelled both for wetting and non-wetting fluids. For the former, the precursor film thickness is a modelling parameter that is not easily measured or known *a priori*.

By performing a stability analysis of the obtained base flows, [60–62] determined the governing dispersion relations and found a dominant wavenumber and corresponding maximum growth rate. The most unstable mode has a wavelength that is approximately three times the width W of

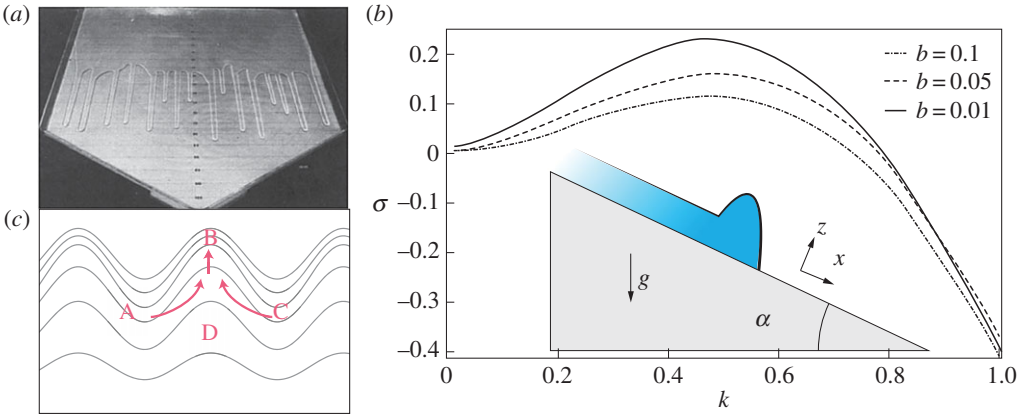

Figure 17. Capillary ridge instability. (*a*) Experimental image from Huppert [59], (*b*) dispersion relation from Spaid & Homsy [62] (inset: typical base flow), (*c*) instability mechanism as drawn by Brenner [61]. (Online version in colour.)

the bump. Figure 17 reproduces one of these dispersion relations as a function of the precursor film thickness. While the trend is very similar, there are still differences in the dispersion relation that result from the differences in base flow. The sensitivity of an eigenvalue to a base flow modification is known to be possibly very high in flows that are non-normal [63], i.e. that have a linear stability operator which does not commute with its adjoint operator. This is often the case in advection-dominated flows. In the present situation, the sensitivity to the precursor film thickness is perceivable but does not alter the main conclusions. This is in stark contrast with wall-bounded shear flows for which a minute change can all of a sudden destabilize the flow [27,63]. Turning back to the capillary ridge instability, the same authors have also considered the effect of a fixed advancing contact angle and obtained very similar dispersion curves, which demonstrates the robustness of the underlying physical mechanism.

Turning to the governing physical mechanism [61,62], the dominant effect is that, under the action of a constant body force, thicker films have less resistance than thinner films, as the velocity scales as the thickness squared. So if the surface is locally more elevated, then it flows faster and is simultaneously replenished from the side, ensuring continuous growth. This lateral flow is best visible from the height levels depicted in figure 17*c*, adapted from [61]. In other words, a transverse perturbation of the flow front develops thicker regions that advance more rapidly. In broad terms, the fluid will tend to follow both the path of least resistance and of steepest descent, and thereby accentuate the fingers. Using a series of scaling arguments to quantify these effects in the linear regime, Brenner [61] has obtained an approximate dispersion relation of the form

$$\omega = 4\mathrm{i}\left(\left(\frac{1}{W^2} + \cot(\alpha)(3Ca)^{1/3}\right)k^2 - k^4\right), \tag{3.106}$$

where k is the transverse wavenumber, W the capillary ridge width, $Ca = \mu U/\gamma$ the capillary number and α the inclination angle. At large inclination, $k_{\max} = 1/2W$ and $\lambda_{\max} = \pi W$ in close agreement to the values reported by the numerical analysis of [60].

It is important to note however that the capillary instability only appears for sufficient inclination, while fingers are also observed in the laboratory at inclination angles below the latter. Bertozzi & Brenner [64] have proposed an original interpretation, based on a transient growth analysis, suggesting that minor variations in topography, in addition to thermal effects, may influence the development of these fingers. In this scenario, the driven contact line acts as an asymptotically stable amplifier (as defined in §3a), which has however a sufficient amplification potential to transform the singlest minor variation in the microscopic contact line region into grown-up fingers in the capillary ridge.

(ii) Transient growth mechanisms

We just encountered a situation where the classical hydrodynamic instability theory, solely based on the computation of eigenvalues, is insufficient to interpret the experimentally measured stability bounds. Frequency response (§3a(vii)), sensitivity to base flow modifications and transient growth are three sides of the same coin: the non-normality of the linear stability operator, as reviewed in [27,63]. They all follow from the non-orthogonality of the eigenmodes of a non-normal operator, rigorously defined by its property not to commute with its adjoint. These recently developed concepts have been applied at length to shear flows, to help resolve the disagreement between predicted linear instability onset and experimental evidence: for Couette flow for instance, theory predicts unconditional stability for any Reynolds number Re while transition to turbulence is observed for $Re \sim 2000$ in the cleanest experiments. Sensitivity analysis, transient growth and harmonic response have all contributed to reconcile these contradictory viewpoints: disturbances sustain intense linear algebraic amplification (but not exponential) until nonlinear effects can set in. Note that even more recently, the discovery of unstable travelling wave solutions, which are attracting in all but one unstable direction, has further helped in building a dynamical system point of view of these flows [65].

However, these tools have found only little echo in interfacial instability analysis. In addition to the previously mentioned analysis of the capillary ridge instability [64], let us mention the interpretation of the instability of buoyant droplets in the creeping flow regime [66] or that of dripping from curved ceilings [67,68].

(iii) Tears of wine

Another peculiar, though daily, manifestation of the driven film instability appears in the formation of the tears of wine [69]. Because of the intense evaporation of alcohol in the vicinity of the contact line, the surface tension locally increases, which starts an ascending Marangoni-driven meniscus climb. This drives more and more liquid out of the bath into the meniscus until the Marangoni force is balanced by gravity. At this distance from the bath, the fluid accumulates into an annular rim which quickly destabilizes.

Although the physical mechanism at the origin of this instability is still debated, the rigorous analysis of [70] seems to rule out the Rayleigh–Plateau instability of the rim initially proposed in [69] while it advocates for a capillary ridge instability mechanism.

(h) Kapitza waves

In the previous section, we described the fingers that form at a driven contact line. There is however another instability that mostly manifests in contrast at small inclination angles and once the flow is fully developed. This instability saturates in the so-called Kapitza waves, that can be easily experienced on a rainy day. In contrast with the fingers observed in the previous section, they are homogeneous along the transverse direction (at least before secondary instabilities arise) and have therefore a purely axial wavenumber $k\mathbf{e}_x$. The saturation of the instability in nonlinear waves and their pairing and transverse secondary instabilities have been studied at length and are summarized in [71]. The purpose of this short section is therefore only to propose the simplest description. As shown already in [72], this instability crucially depends on the detailed hydrodynamics across the viscous layer and cannot be captured by the simplest lubrication models. The fundamental mechanism is again that regions with larger height flow faster. As an initial disturbance propagates, a phase-lag is introduced by inertia such that the restoring force of gravity applies out of phase and further enhances the deformation.

Let us start with the base flow, which is written

$$U(y) = U_0 \left(1 - \frac{y^2}{h^2}\right) \tag{3.107}$$

with $U_0 = \rho g h^2 \sin(\alpha)/2\mu$ the interfacial velocity. The natural non-dimensional numbers associated are the Reynolds number $Re = \rho U_0 h/\mu$ and a Froude number $\mathrm{Fr} = U_0^2/gh\cos(\alpha)$ as the shallow wave velocity is simply $c_{\mathrm{shallow}} = \sqrt{g\cos(\alpha)h}$ because it results from the wall normal component of the restoring gravitational force. The non-dimensional surface tension is measured through a Weber number $\rho U_0^2 h/\gamma$. Instead of solving the linearized Navier–Stokes equations together with the dynamic and kinematic interfacial conditions numerically, it is possible to proceed in the lubrication spirit by considering $kRe \ll 1$. More precisely, following [73], we consider the low wavenumber and low Weber number asymptotic expansion, $k \ll 1$, $Re = \mathcal{O}(1)$ and $\mathrm{We} \sim \alpha^2$. After a systematic algebra, the following approximate dispersion relation is obtained:

$$\omega = \frac{U_0}{h}\left(2kh + \mathrm{i}\frac{8Re}{15}(kh)^2\left(1 - \frac{5}{8}\left(\frac{1}{\mathrm{Fr}} + \frac{(kh)^2}{\mathrm{We}}\right)\right)\right). \tag{3.108}$$

For Froude numbers below a critical Froude number $\mathrm{Fr_c} = \frac{5}{8}$, the flow is stable. However, for $\mathrm{Fr} > \mathrm{Fr_c}$, the dispersion relation has a now familiar $k^2 - k^4$ structure, which displays a cut-off wavenumber $k_c = \sqrt{\mathrm{We}(1/\mathrm{Fr_c} - 1/\mathrm{Fr})}$. In contrast with the Rayleigh–Plateau and Rayleigh–Taylor instabilities, this long wavelength interfacial instability has a characteristic wavelength which decreases with the departure from threshold. Waves with smaller wavelengths are expected to appear at larger Froude numbers. A lubrication based analysis which would include inertia has also been proposed, but it does not yield the correct, numerically predicted, critical Froude number. Various corrections have been proposed, in particular the depth-averaged kinetic energy conservation equations (see [73] for a more thorough description), which were seen to provide the correct growth rate, as well as a series of nested depth-averaged models, reviewed in [71], which were found very useful for the study of nonlinear saturation of the solitary type waves.

(i) Viscous buckling, coiling and folding

Buckling, first explained by Euler in 1757, has since then been a classic topic in solid mechanics. Yet, buckling is not exclusive to elastic rods. Taylor, in his seminal paper on the stability of viscous jets, threads and sheets [74], has revealed that the longitudinal compressive stresses leading to buckling could also be found in fluids, as commonly observed when pouring honey onto toast. In this specific case, the buckling instability further develops in an inherently nonlinear fashion and leads to the formation of patterns: coils and folds (see [75] for references). More intricate shapes are possible when breaking the axisymmetry of the problem, e.g. when the viscous thread falls onto a moving belt or from a nozzle translated in the laboratory frame, a problem called the fluid mechanical sewing machine. Coils, alternating loops and meanders are encountered when increasing the relative speed between nozzle and surface of impact. W-patterns, double coils and other resonant and chaotic patterns are also possible as a token of the richness of the problem that includes viscous stresses (stretching, bending and twisting resistance of the thread), gravitational forces, inertia and surface tension. Of particular interest for this review is that the pattern morphology, e.g. the coiling radius, and the pattern shape *cannot* be captured by traditional means of stability analysis. Instead, a full fledged nonlinear model is needed to account for those shapes, which are produced far from equilibrium [76]. In particular, some nonlinearities are rooted in geometry. For low heights of fall, i.e. when inertia is negligible, the pattern formation may be rationalized in terms of quasi-static model formulated as an evolution problem for the position of the contact point. Specifically, the curvature of the path of the thread's contact point with the belt is that of the thread right before impact, which, in turn, depends on the position and orientation of the thread. This dependence induces a memory effect which explains the complexity of the patterns, as well as they ubiquity: similar coils, loops and meanders are observed with elastic rods, such as ropes, with a remarkably close physical picture [77]. This example shows that stability analysis methods, as described throughout this article, are to be applied with discernment and a critical mind. In particular, in the case of the fluid mechanical sewing machine the pattern formation is formulated in terms of the evolution of the position of

a single point, that is using methods which belong to the field of dynamical systems rather than that of pattern formation [6,77].

4. Harnessing instabilities

In engineering, mechanical instabilities are traditionally associated with the idea of failure. They may induce spurious vibrations, e.g. the rain- and wind-induced vibrations of cable-stayed bridges, or may cause substantial structural damage, e.g. buckled tanks or railroad tracks. As a consequence, instabilities are usually primarily studied with the hope of attenuating or suppressing them. Specifically, the conditions under which instabilities arise have been the focus of extensive research in order to provide design guidelines to avoid them for systems in a variety of fields ranging from civil and mechanical engineering to material science and chemical engineering. In stark contrast with this classic school of thought, we have witnessed—in recent years—the emergence of a paradigm shift in our perception of stability and instabilities. The very same instabilities that were feared are now thought as opportunities to build materials and structures. This burgeoning movement, which was recently formulated in the field of elasticity [81,82], where it led to the development of a variety of meta-materials [83], has been fuelled by developments in soft-matter married to an increased understanding of the far-from-equilibrium elasticity of slender structures. Fluid mechanics too has surfed along on the instability-harnessing [84,85] wave and has the potential of enriching this segment [79,86–88], through pattern forming instabilities in complex media as detailed next.

In this section, we focus on fluidic systems and demonstrate how instabilities—seen as natural evolutions of materials in given environments—are particularly advantageous as they allow the fabrication of periodically structured objects without the need for external assistance. Specifically, we exemplify how instability-mediated pattern formation may be seen as a route to make structures when working with *extreme* materials be it by their size, e.g. in microfabrication and microfluidics, or through the hostile environment where they are found, e.g. in metal- or glass-working settings where conventional tools are hard to implement. Three examples are discussed next illustrating the virtues and limitations of this new trend.

One of microfluidics' main goals—on its path to mature into a profitable biotech industry—is to reconcile *a priori* contradictory objectives: (i) precisely control the microenvironment of a handful of cells or molecules while (ii) delivering high throughput methods to enable statistical methods. A solution to this conundrum is to fabricate droplets, hundreds of thousands of droplets of picolitres to nanolitres in volume, which ideally would form in a *monodisperse* emulsion. Each drop will contain a small amount of biological material, which will evolve independently of the rest of the flock (as it is confined in an immiscible drop). Central to analysis purposes is the need to form drops of identical size, such that the emulated microenvironment is relatively invariant from one drop to the other. Such emulsions are obtained by *destabilization* of the interface between the so-called dispersed phase and another immiscible continuous phase. In these *passive* techniques, the flow field—originating from syringe pumps or from the channel's local slope—promotes the natural growth of the most unstable mode of interfacial deformation. In turn, the instability growth eventually triggers a singularity, typically yielding a topological change via pinch-off, so that a drop is generated. Note that, while it is a singularity that generates these drops, it is in fact the instability that provides the drop 'blueprint', deciding the size of each droplet thereby ensuring the monodispersity of the emulsion. Surfactants, although not strictly necessary to generate drops, are crucial in the process as they prevent the coalescence of newly formed droplets—thereby stabilizing the emulsion and allowing for its packing in crystals such as that shown in figure 18.

Similarly to some of the patterns discussed throughout this article, it is an interfacial instability that sets the size of the droplets produced in the aforementioned microfluidics processes. This instability therefore prescribes the wavelength of the resulting droplet 'crystal', and—as of importance for this type application—warrants its virtually perfect regularity. This particular feature is remarkable given the scale of the problem. Note that this kind of fragmenting instability

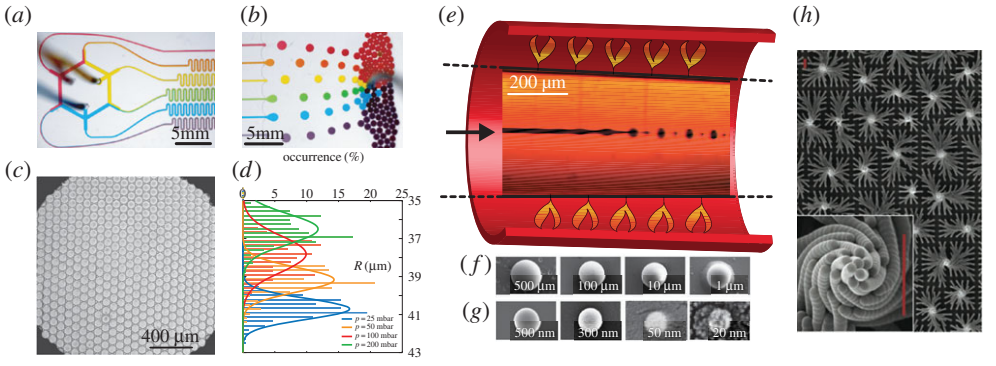

Figure 18. Harnessing instabilities and singularities. The microfluidic rainbow chip connects (*a*) the dispatcher to a (*b*) sloped reservoir yielding the formation of drops, which eventually gather in a (*c*) monodisperse crystal (see (*d*) and [78]). (*e*) A thermal treatment of a fibre allows for the core to melt and, subsequently, destabilize into a series of droplets via the Rayleigh–Plateau instability. (*f*,*g*) Scanning electron microscopy images of such drops, after they cooled down into spherical particles with diameter ranging from 20 nm to 1.4 mm. (Images from (*a–d*) are taken from [78] and (*e–g*) from [79].) (*h*) Helical assemblies [80] generated by the evaporation of an ethanol solvent from a periodic array of nanopillars. Scale bars, 3 µm. (Online version in colour.)

is, of course, not exclusive to microfluidics and is in fact one of the many mechanisms inducing topology changes in fluid mechanics, turning a macroscopic volume of liquid into a collection of fragments via a more or less intricate sequential cascade of breakups [5]. As such, this field has been widely studied and finds use in a variety of applicative settings, e.g. combustion, inkjet printing, etc.

We now turn to a second example described in this section, the in-fibre fabrication of spherical particles obtained by harnessing the Plateau–Rayleigh instability [79]. This example illustrates the practical potential and the modelling challenges of instability-mediated fabrication pathways. The technique relies on the drawing of a preform into a thin multi-material fibre constituted of a cylindrical metalloid core, e.g. silicon, encased in a cladding [79]. The fibre is continuously fed to a heat source, which liquifies the inner core, while the cladding retains its structural integrity. As evident from figure 18*e*, the core–cladding interface is subject to the Rayleigh–Plateau instability, which produces uniformly sized droplets, later *frozen in situ* as the fibre cools down. The size of the drops essentially scales with the radius of the inner core, which—in turn—may be tuned by applying the adequate high-tension redraw process. As a result, spherical particles of radius ranging from 500 µm to 20 nm may be produced (see figure 18*f*,*g*), making this technique an extremely robust avenue of fabrication for particles over a wide range of sizes. This technique, however, poses an interesting challenge to theory. The phase transition of the inner core and the cladding are an inherent part of this dynamical process coupling the thermal problem to the interfacial instability. As a consequence, even if the physical ingredients at play are clearly identified—this is a type of Rayleigh–Plateau interfacial instability—deriving a closed-formed expression for the dispersion relation and eventually *predicting* the size of the particles as a function of the physical parameters of the problem remains unsolved. Some of the aforementioned theoretical tools (the distinction between absolute and convective instabilities) are relevant in this context. However, classical solutions have only been developed for materials whose physical properties are invariant throughout the sample. In this specific case, they fail to predict the adequate wavelength. We argue that this discrepancy is caused by the non-uniformity of the temperature in the fibre. This complication does not change the formal nature of the problem, which remains mathematically well posed. However, temperature gradients make the problem intricate and suited for direct numerical simulations. This set of tools is extremely powerful, yet offers solutions on a case-by-case basis. Given a certain set of initial and boundary conditions one may derive a numerical solution, i.e. drop size in the problem at stake. Solving

the *inverse* problem, that is finding the initial condition that once transmuted by the instability will provide the desired end pattern, remains open when analytical solutions are not available. Trial and error is possible but a generic framework is required and is the current focus of various numerical and theoretical efforts.

In the two previous examples, the instability was mediated by surface tension and was acting directly on a liquid interface so as to fragment it. In this last example, we show that interfacial instabilities are not always destructive, e.g. they can lead to the assembly of pre-existing structures. We focus our attention on the bundles originating from the evaporation of a solvent from a forest of nanopillars [80]. Indeed, slender enough elastic structures are found to undergo large elastic deformations [89] when subject to capillary forces. In the case shown in figure 18*h*, these deformations yield the spontaneous generation of mesoscale hierarchical helical structures in epoxy nanopillars, which are found to pattern the surface of the sample. These artificial coils are possible model systems for a variety of natural systems [80] and have opened the way to capillarity-driven self-organization fabrication pathways [89]. From a mechanistic point of view, this coarsening effect is the result of a destabilization in the elastocapillary interactions in this many-body system. As a result, the patterns depend on both the geometrical properties of the pillars and their initial layout, as well as their physical properties and that of the liquid phase [90]. As such, predicting the final properties of the pattern is not directly attainable by means of a linear stability analysis and more intricate models must be used [90].

5. Conclusion

Patterns in nature have a staggering regularity, which often contrasts with the complexity of their constituents. When attempting to throw pottery, novices soon realize that shaping clay on a wheel requires an extensive skill set and some level of strength. Yet, the unintentional drying of the same clay *automatically* results in cracks at its surface that arrange themselves in an organized tile-like pattern. The apparent *ease* with which such patterns occur suggests that they are encoded in the blueprint of nature and thus spontaneously emerge. In fact, similar patterns are found to cover mud and salt lakes the world over, on kilometric scales.

In this review article, we have used a series of classic fluidic problems as a vehicle to discuss pattern formation and its close relationship with instabilities. Specifically, in the interfacial problems described in this review, we have found that instabilities can be the origin of the pattern's wavelength. The most unstable mode of deformation, which is not necessarily that predicted by a simple temporal instability analysis, tends to surpass all other modes so that a single length scale emerges, thereby enforcing the regularity of the resulting structure. This wavelength, which appears at the onset of the pattern genesis, is then often recovered in the final structure, although often other mechanisms (nonlinear saturation, singularities) enter in the process of finalizing the pattern. As such, linear stability analysis is a powerful tool that enables us to rationalize some of the pattern's features. The main asset of this type of theoretical approach lies in its predictive component. Typically, the dispersion relation derived for a specific problem would exhibit the various non-dimensional groups at work in setting the pattern's wavelength through a formula, ideally an *explicit* formula. In turn, this equation allows one to tame the instability, which may be tailored at will so as to harness its outcome in order to fabricate structures. This unconventional mode of design is elegant as it allows the fabrication of regular structures at the material scale without any direct intervention or dynamic control. As such, this approach—aiming to turn instabilities into the engineer's assistant—is promising. Specifically, it opens possibilities in environments where classical tools are challenged, e.g. micro/nanofabrication, high temperature, etc. Yet, such a fabrication method relies on our ability to both predict and tailor instabilities in order to solve the *inverse problem*, that is to determine the initial condition that, once transmuted by the instability, will produce a desired morphology. In some cases, geometry prevails [88] and thus sets the properties of the instability's outcome, e.g. the pattern wavelength. Further, the physical properties of the material are pushed into the background and leveraging this observation is often sufficient to pilot the instability and have

a complex medium morph into a desired shape [91]. Yet, in more intricate cases, where a phase change is at the heart of pattern formation, further theoretical/numerical efforts would benefit this type of application. The instability and its outcome are found to be sensitive to the detailed properties of a complex medium, which—as implied by its name—are intricate, and thus hard to characterize and model (temperature dependence, shear rate dependence, etc.). Nonetheless, such instabilities lead to remarkably regular structures [87], whose formation is often understood qualitatively by means of analogy with idealized cases. Problems arise with quantitative aspects. Therefore, we expect that improving our ability to predict the outcome of such instabilities, or efficiently solve the inverse problem numerically would pave the way to a new fabrication dogma, that is to tame instabilities in lieu of fearing them. Such an effort is currently observed in fields ranging from mechanics to applied mathematics, to computer graphics and to design and architecture.

To conclude, we note that similar instability-like mechanisms, through a variety of bifurcations, are known to play an active role in living organisms. Further, our capacity to rationalize those instabilities through an improved formalism would benefit our understanding of living matter and inform the development of bioinspired or bio-augmented technology.

Data accessibility. All the data discussed in the article are readily available in the publication.

Authors' contributions. F.G. and P.-T.B. have contributed equally to the article.

Competing interests. The authors have no competing interests.

Funding. F.G. acknowledges the European Research Council for funding the work through a starting grant (ERC SimCoMiCs 280117).

References

1. Thompson DW. 1942 *On growth and form*. Cambridge, UK: Cambridge University Press.
2. Turing AM. 1952 The chemical basis of morphogenesis. *Phil. Trans. R. Soc. Lond. B* **237**, 37–72. (doi:10.1098/rstb.1952.0012)
3. Taylor G. 1950 The instability of liquid surfaces when accelerated in a direction perpendicular to their planes I. *Phil. Trans. R. Soc. Lond. A* **201**, 192–196. (doi:10.1098/rspa.1950.0052)
4. Baron Rayleigh. 1899 *Scientific papers*, vol. 2. Cambridge, UK: Cambridge University Press.
5. Eggers J, Villermaux E. 2008 Physics of liquid jets. *Rep. Progr. Phys.* **71**, 036601. (doi:10.1088/0034-4885/71/3/036601)
6. Cross MC, Hohenberg PC. 1993 Pattern formation outside of equilibrium. *Rev. Mod. Phys.* **65**, 851. (doi:10.1103/RevModPhys.65.851)
7. Chen AS-H, Morris SW. 2013 On the origin and evolution of icicle ripples. *New J. Phys.* **15**, 103012. (doi:10.1088/1367-2630/15/10/103012)
8. Marthelot J, Roman B, Bico J, Teisseire J, Dalmas D, Melo F. 2014 Self-replicating cracks: a collaborative fracture mode in thin films. *Phys. Rev. Lett.* **113**, 085502. (doi:10.1103/PhysRevLett.113.085502)
9. Claudin P, Jarry H, Vignoles G, Plapp M, Andreotti B. 2015 Physical processes causing the formation of penitentes. *Phys. Rev. E* **92**, 033015. (doi:10.1103/PhysRevE.92.033015)
10. Li B, Cao Y-P, Feng X-Q, Gao H. 2012 Mechanics of morphological instabilities and surface wrinkling in soft materials: a review. *Soft Matter* **8**, 5728–5745. (doi:10.1039/c2sm00011c)
11. De Gennes P-G, Brochard-Wyart F, Quéré D 2013 *Capillarity and wetting phenomena: drops, bubbles, pearls, waves*. Berlin, Germany: Springer Science & Business Media.
12. Delaunay CH. 1841 Sur la surface de révolution dont la courbure moyenne est constante. *J. Math. Pures Appl.* **6**, 309–314.
13. Park C-W, Homsy GM. 1984 Two-phase displacement in Hele Shaw cells: theory. *J. Fluid Mech.* **139**, 291–308. (doi:10.1017/S0022112084000367)
14. Nagel M, Brun P-T, Gallaire F. 2014 A numerical study of droplet trapping in microfluidic devices. *Phys. Fluids* **26**, 032002. (doi:10.1063/1.4867251)
15. Huerre P, Monkewitz PA. 1990 Local and global instabilities in spatially developing flows. *Annu. Rev. Fluid Mech.* **22**, 473–537. (doi:10.1146/annurev.fl.22.010190.002353)
16. Huerre P, Rossi M. 1998 Hydrodynamic instabilities in open flows. In *Hydrodynamic and nonlinear instabilities* (eds C Godrèche, P Manneville), pp. 81–294. Cambridge, UK: Cambridge University Press.

17. Eggers J, Dupont TF. 1994 Drop formation in a one-dimensional approximation of the Navier–Stokes equation. *J. Fluid Mech.* **262**, 205–221. (doi:10.1017/S0022112094000480)
18. Duprat C, Ruyer-Quil C, Kalliadasis S, Giorgiutti-Dauphiné F. 2007 Absolute and convective instabilities of a viscous film flowing down a vertical fiber. *Phys. Rev. Lett.* **98**, 244502. (doi:10.1103/PhysRevLett.98.244502)
19. Duclaux V, Clanet C, Quéré D. 2006 The effects of gravity on the capillary instability in tubes. *J. Fluid Mech.* **556**, 217–226. (doi:10.1017/S0022112006009505)
20. Duprat C. 2009 Instabilities of a liquid film flowing down a vertical fibre. Thesis, Université Pierre et Marie Curie, Paris, France.
21. Brun P-T, Damiano A, Rieu P, Balestra G, Gallaire F. 2015 Rayleigh-Taylor instability under an inclined plane. *Phys. Fluids* **27**, 084107. (doi:10.1063/1.4927857)
22. Van Saarloos W. 2003 Front propagation into unstable states. *Phys. Rep.* **386**, 29–222. (doi:10.1016/j.physrep.2003.08.001)
23. Rabaud M, Couder Y. 1983 A shear-flow instability in a circular geometry. *J. Fluid Mech.* **136**, 291–319. (doi:10.1017/S0022112083003177)
24. Doaré O, de Langre E. 2006 The role of boundary conditions in the instability of one-dimensional systems. *Eur. J. Mech. B/Fluids* **25**, 948–959. (doi:10.1016/j.euromechflu.2006.01.001)
25. Gallaire F, Chomaz J-M. 2004 The role of boundary conditions in a simple model of incipient vortex breakdown. *Phys. Fluids* **16**, 274–286. (doi:10.1063/1.1630326)
26. Nichols J, Chomaz JM, Schmid PJ. 2009 Twisted absolute instability in lifted flames. *Phys. Fluids* **21**, 015110. (doi:10.1063/1.3068758)
27. Schmid PJ, Henningson DS. 2001 *Stability and transition in shear flows*. Berlin, Germany: Springer.
28. Chomaz JM, Couairon A. 1999 Against the wind. *Phys. Fluids* **11**, 2977–2983. (doi:10.1063/1.870157)
29. Pier B, Huerre P, Chomaz J-M. 2001 Bifurcation to fully nonlinear synchronized structures in slowly varying media. *Phys. D* **148**, 49–96. (doi:10.1016/S0167-2789(00)00146-9)
30. Fauve S. 1998 Pattern forming instabilities. In *Hydrodynamic and nonlinear instabilities* (ed. C Godrèche, P Manneville), pp. 387–491. Cambridge, UK: Cambridge University Press.
31. Rubio-Rubio M, Sevilla A, Gordillo JM. 2013 On the thinnest steady threads obtained by gravitational stretching of capillary jets. *J. Fluid Mech.* **729**, 471–483. (doi:10.1017/jfm.2013.322)
32. Javadi A, Eggers J, Bonn D, Habibi M, Ribe NM. 2013 Delayed capillary breakup of falling viscous jets. *Phys. Rev. Lett.* **110**, 144501. (doi:10.1103/PhysRevLett.110.144501)
33. Heifetz E, Methven J. 2005 Relating optimal growth to counterpropagating Rossby waves in shear instability. *Phys. Fluids* **17**, 064107. (doi:10.1063/1.1937064)
34. Miles JW. 1957 On the generation of surface waves by shear flows. *J. Fluid Mech.* **3**, 185–204. (doi:10.1017/S0022112057000567)
35. Villermaux E. 1998 On the role of viscosity in shear instabilities. *Phys. Fluids* **10**, 368–373. (doi:10.1063/1.869529)
36. Plesset MS, Whipple CG. 1974 Viscous effects in Rayleigh-Taylor instability. *Phys. Fluids* **17**, 1–7. (doi:10.1063/1.1694570)
37. Chandrasekhar S. 1961 *Hydrodynamic and hydromagnetic stability*. Oxford, UK: Clarendon Press.
38. Limat L. 1993 Instabilité d'un liquide suspendu sous un surplomb solide: influence de l'épaisseur de la couche. *C. R. Acad. Sci.* **317**, 563–568.
39. Fermigier M, Limat L, Wesfreid JE, Boudinet P, Quilliet C. 1992 Two-dimensional patterns in Rayleigh-Taylor instability of a thin layer. *J. Fluid Mech.* **236**, 349–383. (doi:10.1017/S0022112092001447)
40. Lister JR, Rallison JM, Rees SJ. 2000 The nonlinear dynamics of pendent drops on a thin film coating the underside of a ceiling. *J. Fluid Mech.* **647**, 239–264. (doi:10.1017/S002211201000008X)
41. Benjamin TB, Ursell F. 1954 The stability of the plane free surface of a liquid in vertical periodic motion. *Proc. R. Soc. Lond. A* **225**, 505–515. (doi:10.1098/rspa.1954.0218)
42. Douady S. 1990 Experimental study of the Faraday instability. *J. Fluid Mech.* **221**, 383–409. (doi:10.1017/S0022112090003603)
43. Edwards WS, Fauve S. 1994 Patterns and quasi-patterns in the Faraday experiment. *J. Fluid Mech.* **278**, 123–148. (doi:10.1017/S0022112094003642)

44. Case KM, Parkinson WC. 1957 Damping of surface waves in an incompressible liquid. *J. Fluid Mech.* **2**, 172–184. (doi:10.1017/S0022112057000051)
45. Hocking LM. 1987 The damping of capillary-gravity waves at a rigid boundary. *J. Fluid Mech.* **179**, 253–266. (doi:10.1017/S0022112087001514)
46. Miles JW. 1967 Surface-wave damping in closed basins. *Proc. R. Soc. Lond. A* **297**, 459–475. (doi:10.1098/rspa.1967.0081)
47. Viola F, Brun P-T, Dollet B, Gallaire F. 2016 Foam on troubled water: capillary induced finite-time arrest of sloshing waves. *Phys. Fluids* **28**, 091701. (doi:10.1063/1.4961260)
48. Pearson JRA. 1958 On convection cells induced by surface tension. *J. Fluid Mech.* **4**, 489–500. (doi:10.1017/S0022112058000616)
49. Manneville P. 2006 Rayleigh-Bénard convection, thirty years of experimental, theoretical and modeling work. In *Dynamics of spatio-temporal structures—Henri Bénard centenary review* (eds. I Mutabazi, E Guyon, JE Wesfreid), Berlin, Germany: Springer.
50. Newell AC, Whitehead JA. 1969 Finite bandwidth, finite amplitude convection. *J. Fluid Mech.* **38**, 279–303. (doi:10.1017/S0022112069000176)
51. Segel LA. 1969 Distant side-walls cause slow amplitude modulation of cellular convection. *J. Fluid Mech.* **38**, 203–224. (doi:10.1017/S0022112069000127)
52. Carrière JP, Monkewitz PA. 1999 Convective versus absolute instability in mixed Rayleigh-Bénard-Poiseuille convection. *J. Fluid Mech.* **384**, 243–262. (doi:10.1017/S0022112098004145)
53. Martinand D, Carrière JP, Monkewitz PA. 2004 Envelope equations for the Rayleigh-Bénard-Poiseuille system. Part 2. Linear global modes in the case of two-dimensional non-uniform heating. *J. Fluid Mech.* **502**, 175–197. (doi:10.1017/S002211200300778X)
54. Couder Y. 2000 Viscous fingering as an archetype of growth pattern. In *Perpectives in fluid dynamics* (eds GK Batchelor, HK Moffatt, MG Worster), pp. 53–104. Cambridge, UK: Cambridge University Press.
55. Saffman PG, Taylor GI. 1958 The penetration of a fluid into a porous medium or Hele-Shaw cell containing a more viscous liquid. *Proc. R. Soc. Lond. A* **245**, 312–329. (doi:10.1098/rspa.1958.0085)
56. Bischofberger I, Ramachandran R, Nagel SR. 2014 Fingering versus stability in the limit of zero interfacial tension. *Nat. Commun.* **5**, 5265. (doi:10.1038/ncomms6265)
57. Leal LG. 2007 *Advanced transport phenomena: fluid mechanics and convective transport processes*. Cambridge, UK: Cambridge University Press.
58. Nagel M, Gallaire F. 2013 A new prediction of wavelength selection in radial viscous fingering involving normal and tangential stresses. *Phys. Fluids* **25**, 124107. (doi:10.1063/1.4849495)
59. Huppert H. 1982 Flow and instability of a viscous current down a slope. *Nature* **300**, 427–429. (doi:10.1038/300427a0)
60. Troian SM, Herbolzheimer E, Safran SA, Joanny JF. 1989 Fingering instabilities of driven spreading films. *Europhys. Lett.* **10**, 25–30. (doi:10.1209/0295-5075/10/1/005)
61. Brenner MP. 1993 Instability mechanism at driven contact lines. *Phys. Rev. E* **47**, 4597–4599. (doi:10.1103/PhysRevE.47.4597)
62. Spaid MA, Homsy GM. 1996 Stability of newtonian and viscoelastic dynamic contact lines. *Phys. Fluids* **8**, 460–478. (doi:10.1063/1.868800)
63. Chomaz J-M. 2005 Global instabilities in spatially developing flows: non-normality and nonlinearity. *Annu. Rev. Fluid Mech.* **37**, 357–392. (doi:10.1146/annurev.fluid.37.061903.175810)
64. Bertozzi AL, Brenner MP. 1997 Linear stability and transient growth in driven contact lines. *Phys. Fluids* **9**, 530–539. (doi:10.1063/1.869217)
65. Eckhardt B, Schneider TM, Hof B, Westerweel J. 2007 Turbulence transition in pipe flow. *Annu. Rev. Fluid Mech.* **39**, 447–468. (doi:10.1146/annurev.fluid.39.050905.110308)
66. Gallino G, Zhu L, Gallaire F. 2016 The stability of a rising droplet: an inertialess non-modal growth mechanism. *J. Fluid Mech.* **786**, R2. (doi:10.1017/jfm.2015.650)
67. Trinh PH, Kim H, Hammoud N, Howell PD, Chapman SJ, Stone HA. 2014 Curvature suppresses the Rayleigh-Taylor instability. *Phys. Fluids* **26**, 051704. (doi:10.1063/1.4876476)
68. Balestra G, Brun P-T, Gallaire F. 2016 Rayleigh-Taylor instability under curved substrates: an optimal transient growth analysis. *Phys. Rev. Fluids* **1**, 083902. (doi:10.1103/PhysRevFluids.1.083902)
69. Cazabat A-M, Heslot F, Troia S, Carles P. 1990 Fingering instability of thin spreading films driven by temperature gradients. *Nature* **346**, 824–826. (doi:10.1038/346824a0)

70. Kataoka DE, Troian SM. 1997 A theoretical study of instabilities at the advancing front of thermally driven coating films. *J. Colloid Interface Sci.* **192**, 350–362. (doi:10.1006/jcis.1997.5018)
71. Kalliadasis S, Ruyer-Quil C, Scheid B, Velarde MG. 2012 Falling liquid films. Applied Mathematical Sciences, vol. 176. London, UK: Springer. (doi:10.1007/978-1-84882-367-9)
72. Yih CS. 1963 Stability of liquid flow down an inclined plane. *Phys. Fluids* **6**, 321–334. (doi:10.1063/1.1706737)
73. Charru F 2011 *Hydrodynamic instability*. Cambridge, UK: Cambridge University Press.
74. Taylor GI. 1969 Instability of jets, threads, and sheets of viscous fluid. In *Applied mechanics*, pp. 382–388. Berlin, Germany: Springer.
75. Ribe NM, Habibi M, Bonn D. 2012 Liquid rope coiling. *Annu. Rev. Fluid Mech.* **44**, 249–266. (doi:10.1146/annurev-fluid-120710-101244)
76. Audoly B, Clauvelin N, Brun P-T, Bergou M, Grinspun E, Wardetzky M. 2013 A discrete geometric approach for simulating the dynamics of thin viscous threads. *J. Comput. Phys.* **253**, 18–49. (doi:10.1016/j.jcp.2013.06.034)
77. Brun P-T, Audoly B, Ribe NM, Eaves TS, Lister JR. 2015 Liquid ropes: a geometrical model for thin viscous jet instabilities. *Phys. Rev. Lett.* **114**, 174501. (doi:10.1103/PhysRevLett.114.174501)
78. Dangla R, Kayi SC, Baroud CN. 2013 Droplet microfluidics driven by gradients of confinement. *Proc. Natl Acad. Sci. USA* **110**, 853–858. (doi:10.1073/pnas.1209186110)
79. Kaufman JJ, Tao G, Shabahang S, Banaei E-H, Deng DS, Liang X, Johnson SG, Fink Y, Abouraddy AF. 2012 Structured spheres generated by an in-fibre fluid instability. *Nature* **487**, 463–467. (doi:10.1038/nature11215)
80. Pokroy B, Kang SH, Mahadevan L, Aizenberg J. 2009 Self-organization of a mesoscale bristle into ordered, hierarchical helical assemblies. *Science* **323**, 237–240. (doi:10.1126/science.1165607)
81. Reis PM. 2015 A perspective on the revival of structural (in) stability with novel opportunities for function: from buckliphobia to buckliphilia. *J. Appl. Mech.* **82**, 111001. (doi:10.1115/1.4031456)
82. Reis PM, Jaeger HM, van Hecke M. 2015 Designer matter: a perspective. *Extreme Mech. Lett.* **5**, 25–29. (doi:10.1016/j.eml.2015.09.004)
83. Babaee S, Shim J, Weaver JC, Chen ER, Patel N, Bertoldi K. 2013 3D soft metamaterials with negative Poisson's ratio. *Adv. Mater.* **25**, 5044–5049. (doi:10.1002/adma.201301986)
84. McKinley GH. 2005 Visco-elasto-capillary thinning and break-up of complex fluids. *Rheol. Rev.* 1–48.
85. Martin GD, Hoath SD, Hutchings IM. 2008 Inkjet printing—the physics of manipulating liquid jets and drops. *J. Phys. Conf. Ser.* **105**, 012001. (doi:10.1088/1742-6596/105/1/012001)
86. Kaufman JJ *et al*. 2013 In-fiber production of polymeric particles for biosensing and encapsulation. *Proc. Natl Acad. Sci. USA* **110**, 15 549–15 554. (doi:10.1073/pnas.1310214110)
87. Gumennik A *et al*. 2013 Silicon-in-silica spheres via axial thermal gradient in-fibre capillary instabilities. *Nat. Commun.* **4**, 2216. (doi:10.1038/ncomms3216)
88. Passieux R, Guthrie L, Rad SH, Lévesque M, Therriault D, Gosselin FP. 2015 Instability-assisted direct writing of microstructured fibers featuring sacrificial bonds. *Adv. Mater.* **27**, 3676–3680. (doi:10.1002/adma.201500603)
89. Roman B, Bico J. 2010 Elasto-capillarity: deforming an elastic structure with a liquid droplet. *J. Phys. Condens. Matter* **22**, 493101. (doi:10.1088/0953-8984/22/49/493101)
90. Wei Z, Schneider TM, Kim J, Kim HY, Aizenberg J, Mahadevan L. 2015 Elastocapillary coalescence of plates and pillars. *Proc. R. Soc. A* **471**, 20140593. (doi:10.1098/rspa.2014.0593)
91. Brun P-T, Audoly B, Ribe NM, Eaves TS, Lister JR. 2015 Liquid ropes: a geometrical model for thin viscous jet instabilities. *Phys. Rev. Lett.* **114**, 174501. (doi:10.1103/PhysRevLett.114.174501)